IEEE Access
Multidisciplinary ⋮ Rapid Review ⋮ Open Access Journal

Received 9 April 2023, accepted 27 April 2023, date of publication 5 May 2023, date of current version 18 May 2023.

Digital Object Identifier 10.1109/ACCESS.2023.3273297

RESEARCH ARTICLE

Reconfigurable Intelligent Surface-Aided Orthogonal Time Frequency Space and Its Deep Learning-Based Signal Detection

MAHMUDUL HASAN ABID, IFFAT ARA TALIN, AND MOHAMMAD ISMAT KADIR, (Senior Member, IEEE)
Electronics and Communication Engineering Discipline, Khulna University, Khulna 9208, Bangladesh
Corresponding author: Mohammad Ismat Kadir (ismat.kadir@ece.ku.ac.bd)

The research has been funded by the Research and Innovation Centre of Khulna University, Bangladesh.

ABSTRACT Orthogonal time frequency space (OTFS) has emerged as a promising modulation for next-generation wireless systems. This two-dimensional (2D) modulation has the inherent capability of providing uninterrupted connectivity and improved performance in a high-mobility doubly-selective channel by mapping the information symbols to the delay-Doppler (DD) domain. In order to improve the directivity of OTFS signals, this paper considers a reconfigurable intelligent surface (RIS)-aided OTFS transmission for a high-speed environment. While OTFS mitigates the dispersion due to the highly mobile wireless channels by mapping the transmit symbols to the DD domain, RIS improves the directivity by appropriately shifting the phase of the signal in non-line-of-sight (NLOS) communication channels. We provide a concrete matrix-based mathematical model of the RIS-aided OTFS communication system. Capitalizing on the simple matrix multiplication-based model, a number of detectors can be used. These include the usual zero-forcing (ZF) and the minimum mean-squared error (MMSE) linear detectors, and a low-complexity message passing algorithm (MPA)-assisted detector. We evaluate the performance of these detectors for RIS-based OTFS systems. A deep learning (DL)-based signal detector is also proposed for the RIS-aided OTFS system. A significant improvement in bit-error-rate (BER) performance is achieved using the system considered, while the RIS-induced computational burden is not high. Furthermore, in NLOS communication, our system can ensure seamless connectivity with a reduced number of base stations (BS).

INDEX TERMS Reconfigurable intelligent surface (RIS), orthogonal time frequency space (OTFS), deep learning (DL), doubly selective channels.

I. INTRODUCTION

With the advancement of wireless communications, numerous modulation techniques have been developed to meet the next-generation requirements. Network requirements have also become stringent as well over time. The next-generation wireless networks will have to satisfy the requirements of data transmissions indoors and outdoors. Additionally, these networks will have to support communication in densely populated areas, mobile broadband services in high-mobility vehicles, for example, airplanes, internet of things (IoT), and others. High-speed data transmissions may be accomplished by high carrier frequencies, network densification, and/or by new access methods for spectral efficiency enhancement [1], [2]. Orthogonal frequency-division multiplexing (OFDM) was considered as modulation of choice for European Digital Audio Broadcasting (DAB) [3] and the Digital Video Broadcasting (DVB) [4], and HIPERLAN/2 [5]. OFDM was chosen for its ability to provide high spectral efficiency, whilst combating the inter-symbol interference (ISI) imposed by dispersive wireless channels [6], [7]. OFDM was also found suitable for multi-user multi-antenna scenarios [8], [9]. However, in the context of the more complex network required for the next-generation wireless systems

The associate editor coordinating the review of this manuscript and approving it for publication was Anandakumar Haldorai.

where Doppler shifts of different users are high or cannot be accurately predicted, OFDM has to face the challenges imposed by timing- and carrier frequency offsets and by the out-of-band (OOB) emissions [10]. The Doppler shift present in the channel degrades the orthogonality between the subcarrier frequencies, thus increasing the inter-carrier interference (ICI) of the network [11], [12]. To mitigate the ICI-related problems due to a doubly selective channel, there are numerous attempts [13], [14], [15], [16], [17] in the literature, Additionally, to overcome the synchronization problem and the OOB emissions, several modulation techniques, for example, filter-bank multicarrier (FBMC) [18], universal filtered multi-carrier (UFMC) [19], and generalized frequency division multiplexing (GFDM) [20] were proposed. However, these modulations cannot effectively mitigate channel dispersion due to the high mobility of users.

Against this background, orthogonal time frequency space (OTFS) [21], [22] was proposed. OTFS is an *avant-garde* modulation format, which changes the conventional mechanism of mapping the information symbols. Traditionally, the symbols are mapped to the time or frequency domain, whereas OTFS maps the symbols to the delay-Doppler (DD) domain. OTFS is an ingenious two-dimensional (2D) modulation approach that empowers the doubly selective channel to have orthogonality and separability between carrier waveforms allowing highly dispersive gain [23], [24], [25], [26]. The exclusiveness of this DD representation of the signal is that it embodies two opposite ideas. According to Heisenberg's uncertainty principle, a signal can not be simultaneously localized in both time and frequency. Without violating Heisenberg's uncertainty principle, an OTFS-modulated signal behaves as if it is simultaneously localized in both the time and frequency domain. This unique characteristic is achieved through maintaining the 'quasi periodicity' of the OTFS carrier [22], [27]. OTFS can provide improved performance in high-mobility channels as well as static multipath channels [24], [28]. The performance of OTFS was compared with that of OFDM in [29], [30], and [31] for high-mobility channels, and OTFS was observed to outperform OFDM.

To ensure high-speed ubiquitous connectivity, we have to face some more impediments. Firstly, we have to guarantee seamless network coverage both indoors and outdoors. In addition to the line of sight (LOS) propagation, random natural and man-made entities such as buildings, trees, vehicles, mountains, etc. hinder the propagation in non-line of sight (NLOS) communication. Uncontrollable interactions of the transmitted signal with surrounding random objects contribute to multipath interference and degrade the quality of the received signals [32], [33]. The main propagation challenges are deep fading, ISI, severe attenuation, and high Doppler shifts [34]. Although a good number of physical layer (PHY) solutions, for example, adaptive modulation and coding (AMC), cooperative communications, multicarrier modulation, and large-scale multiple-input multiple-output (LS-MIMO) have emerged, the improvements in the PHY are not sufficient to provide maximum capacity and required reliability. Furthermore, as the propagation medium is unpredictable, the implemented technologies can not ensure the quality of service (QoS) of the network. As a solution, the idea of employing a reconfigurable intelligent surface (RIS) has recently attracted substantial interest. RISs are placed in between the transmitter and the receiver, and can strategically configure and redirect the radio signal impinged on it. The design and fabrication details of RIS are detailed in [35].

The ideal operation of RIS is considered by analyzing a perfectly conducting plate all by itself. This passive surface behaves as a reflecting mirror for incoming radio waves by scattering the incoming signal to an angle determined by the *generalized Snell's law of reflection* [36], [37]. However, it is necessary to attain 'anomalous reflections' [38] in order to serve a system where the transmitter or receiver or both is non-stationary. Instead of using a single continuous reflecting element, a practical RIS surface is constituted with a finite number of software-controlled passive elements. Each of the elements adapts a constant phase shift based on the position of the desired user to provide directive reflection [39], [40]. The properties of the individual elements can be controlled by a switching device, which is further controlled by a microcontroller. The RIS enabled by the microcontroller automatically redirects the incident signal to a specific user even in mobile conditions [41]. By varying the characteristics of the components, the impedance of the elements may be varied, resulting in a phase shift of the signals impinging on the surface. The RIS operates in two fundamental strategies: the energy-focusing mode and energy-nulling mode [36], [42], [43]. In energy-focusing mode, appropriate phase shifts are provided by each passive element with the help of a microcontroller in order to provide focused beamforming to the desired user by constructively adding the phase shifts of the individual elements. In the energy-nulling strategy, the signal received by any user other than the desired user is destructively added with an appropriate phase shift to nullify the overall effect of co-channel interference. In this way, microcontroller-operated RIS can function as a reconfigurable lens that focuses the incident signal to the desired user and ensures directive gain [34], [44]. Recently, a resonant coupling-based RIS unit was designed by utilizing the characteristics of PIN diode for phase controlling [45]. This technique utilized microstrip and meander antenna theory and achieved lower loss along with broadband capacity. RIS has been proven in studies to enhance network coverage, data transmission speed, and energy efficiency while maintaining an effective cost margin [46], [47]. RIS can improve the rank of a LOS system by adding multipath, thus improving the capacity gain [48]. In [44], the SNR behavior of RIS was analyzed in the context of LS-MIMO systems. In the far field, the SNR of RIS grows quadratically as a function of the number of elements. However, in the near field, the SNR performance of RIS significantly degrades. The analysis of [44] suggests

that RIS of a greater number of elements than the array size in the LS-MIMO system can resolve the issue of SNR degradation. Configuring the propagation medium with decode-and-forward (DF) relaying is another popular choice [49]. In [50], the authors showed that a hundred-element RIS can outperform DF in terms of energy efficiency and the transmitting power of the signal. The performance of a RIS-assisted channel is determined by its ability to provide accurate phase shift and the channel path-loss to the desired user [36]. The accuracy of the phase shift is dependent on the size and the number of passive elements. In general, the elements are of the sub-wavelength size in order to provide precise directivity of the scattered signal [36]. By contrast, the path-loss depends on the net size of the RIS surface rather than the sizes of the individual elements. The beam width of the reflected signal is inversely proportional to the size of the RIS surface [36]. RIS has been implemented in numerous applications. For example, a RIS-assisted system was proposed for Industrial IoT (IIoT) systems, that demonstrated significant performance enhancement even in scenarios with high interference and limited spectrum availability [51].

The majority of RIS research studies have taken a static environment into account. Recently this has also been implemented in channels with high mobility [52], [53], [54]. In particular, in the papers [52], [53], and [55] a doubly selective channel with a high Doppler spread has been taken into consideration for RIS-assisted OTFS communication. However, a straight-forward matrix multiplication-based system model for RIS-aided OTFS communicating in high-mobility dispersive scenarios and the design of an appropriate detector for this system is unexplored. In this research, we explored three types of conventional detectors, namely- linear zero-forcing (ZF) or minimum mean-squared error (MMSE) detectors, maximum *a posteriori* (MAP) detectors [24], [54], [56], [57], and designed a machine learning-aided detector for the proposed RIS-aided OTFS system. As far our knowledge, machine learning-based detection for the RIS-assisted OTFS system has not been studied yet.

Specifically, our contributions may be summarized as follows:

1) We propose a deep neural network (DNN) based detector for the RIS-assisted OTFS system considered for communications over doubly selective high-speed channels.
2) We provide a simple matrix multiplication-based model for a RIS-aided OTFS scheme communicating in a hostile environment characterized by a doubly selective channel.
3) The shapes of the channel transfer matrix in both the time domain (TD) and the DD domain for OTFS with or without RIS are characterized. The performance of the system using the proposed DL-based detector has been investigated and compared with that employing ZF, MMSE, and message passing (MP)-based detectors and with that of OFDM using similar parameter values. The system considered in conjunction with the proposed detector provides significantly improved performance compared to the benchmark schemes.

The RIS-aided OTFS scheme is capable of simultaneously providing higher directive gain and mitigating the channel-induced dispersion in a hostile environment. In general, the higher the directive gain of a scheme, the less its capability to overcome channel-induced dispersion. The system can benefit from the simultaneous use of RIS and OTFS and thus stands out to be a promising solution for next-generation ultra-reliable systems.

A. OUTLINE

The paper is organized as follows. In Section II, the transceiver architecture of the RIS-aided OTFS system is detailed. The straightforward matrix multiplication-based model is also derived in this section. Section III discusses the proposed DL-based detector for the RIS-aided OTFS system. The complexity imposed by the proposed DL-based detector and by the conventional detectors are compared in Section IV. In Section V, the system is studied using numerical simulations. Section V also discusses the limitations of the study and outlines some potential future works. Finally, we conclude the paper in Section VI.

B. NOTATIONS

In general, we use boldface letters such as $\boldsymbol{A}$ to denote a vector or a matrix, whereas $\boldsymbol{A}^{-1}$, $\boldsymbol{A}^{T}$, $\boldsymbol{A}^{H}$ represent the inverse, transpose, and Hermitian transpose of a matrix, respectively. The Kronecker product of two matrices $\boldsymbol{A}$ and $\boldsymbol{B}$ is denoted by $\boldsymbol{A}\otimes\boldsymbol{B}$, the convolution of two vectors by $*$, the $M\times M$ identity matrix by $\boldsymbol{I}_M$, while $\boldsymbol{\mathcal{F}}_N$ and $\boldsymbol{\mathcal{F}}_N^H$ denote the N-point discrete Fourier transform (DFT) matrix and the N-point inverse DFT (IDFT) matrix, respectively.

II. SYSTEM OVERVIEW

Fig. 1 portrays an overview of the RIS-aided OTFS scheme. We consider a source-to-user communication scenario over a high-mobility doubly selective channel. A RIS is positioned in between the source and the destination user in order to provide reconfigurable directivity to the destination. We consider a RIS consisting of K processing elements and their phases may be controlled in accordance with requirements at the receiver. The communication from the source to a single user is illustrated in Fig. 1 for the sake of simplicity. Communication with other users - may be mobile or stationary - can be performed in a similar fashion. Although there may exist a direct line-of-sight (LOS) link, these links are seldom available for long-distance high-speed vehicular communications or in mobile hotspots, for example, railway stations and busy airports. Hence, we consider the source information to be OTFS modulated in both the source-to-RIS and the RIS-to-destination links. We also consider the K-element RIS to have a smart controller which ensures directive gain to the desired user by offering an appropriate

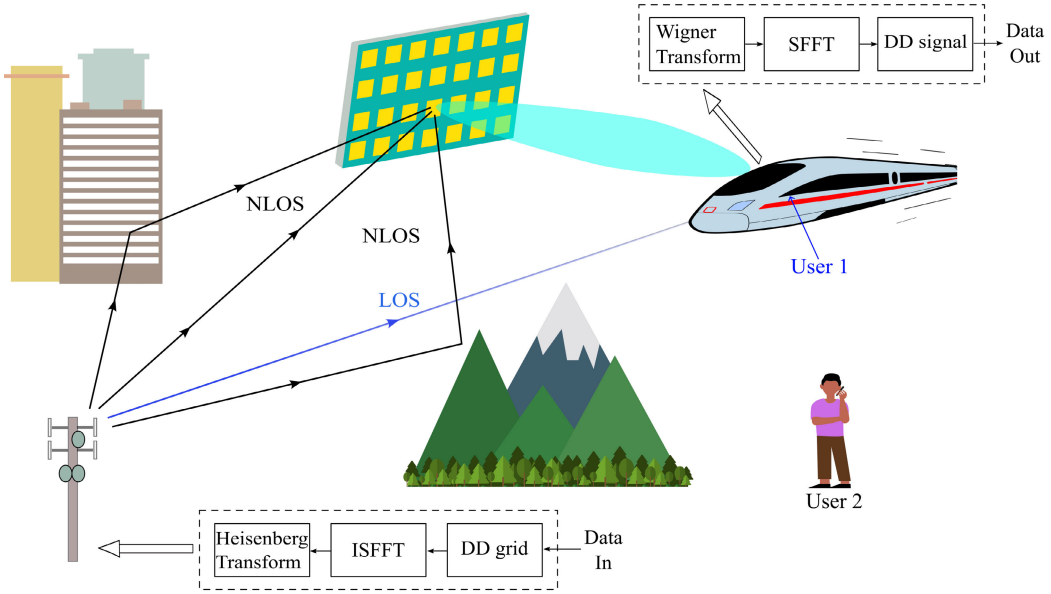

FIGURE 1. Overview of the RIS-aided OTFS system. The source information is OTFS-modulated, and appropriately phase-shifted at the RIS to reach the destination, where it is OTFS-demodulated and detected.

phase shift to the incident signal. The phase-shifted incident signal or the reflected time-domain signal reaches the desired user and is demodulated at the receiver side.

A. OTFS MODULATION AT THE TRANSMITTER

At the transmitter end, at first, OTFS modulation is applied to the source information. As described, OTFS modulation is the process of mapping the information symbol into a 2D grid. In OTFS modulation, instead of using the 1D time-frequency (TF) grids, the source bits are first translated to a set of $\mathcal{L}-$QAM symbols, and then the resulting QAM symbols are translated into a 2D grid, called DD grids. We consider the OTFS transmit frames consists of $(M \times N)$ number of $\mathcal{L}-$QAM symbols that are mapped to DD symbols $\boldsymbol{X} \in \mathbb{C}^{M\times N}$. Explicitly, the total duration of the signal frame is assumed to be NT and the sampling interval is MT, where T denotes the pulse duration. We consider integer delay and Doppler scenario as opposed to fractional delay-Doppler [53].

For wireless transmission, TD signal is needed. Using a two-step conversion method, the DD symbols are transformed into TD signal-

1) At first, the DD symbols are transformed into TF signal using inverse symplectic Fourier transform (ISFFT). The ISFFT operation is implemented by applying $M-$point fast Fourier transform (FFT) and then the $N-$point inverse fast Fourier transform (IFFT) across the columns and rows of the DD transmit frame $\boldsymbol{X}$, respectively.
2) Then the TF signal is transformed into TD signal using the Heisenberg transform. An $M-$point IFFT is used in conjunction with a pulse-shaping waveform to achieve this.

Assuming rectangular pulse shaping, the OTFS-modulated TD transmit signal can be expressed as [58], [59], [60]:

$$\boldsymbol{S} = \boldsymbol{F}_M^H \left(\boldsymbol{F}_M \boldsymbol{X} \boldsymbol{F}_N^H\right) = \boldsymbol{X}\boldsymbol{F}_N^H. \tag{1}$$

The TD transmit matrix $\boldsymbol{S} \in \mathbb{C}^{M\times N}$ can be converted to a TD vector $\boldsymbol{s} \in \mathbb{C}^{MN\times 1}$ by:

$$\begin{aligned} \boldsymbol{s} &= \text{vec}\,(\boldsymbol{S}) \\ &= \left(\boldsymbol{F}_N^H \otimes I_M\right) \text{vec}\,(\boldsymbol{X}) \\ &= \left(\boldsymbol{F}_N^H \otimes I_M\right) \boldsymbol{x}, \end{aligned} \tag{2}$$

where vec $(\bullet)$ denotes the column-wise vectorial stacking operation on the matrix '$\bullet$'.

As a further advance, we append a cyclic prefix (CP) of appropriate length to mitigate inter-symbol interference (ISI). However, we use a single cyclic prefix per frame to increase the overall spectral efficiency [58], [59], [60].

B. SOURCE-TO-RIS AND RIS-TO-DESTINATION CHANNEL

We consider both the source-to-RIS and the RIS-to-destination links to be doubly selective. The complex baseband channel impulse response (CIR) $h(\tau, \nu)$ of each link is assumed to have a delay denoted by τ and a Doppler shift denoted by ν, and the CIR may be expressed by [13], [24], [26], [33], [58]:

$$h(\tau, \nu) = \sum_{i=0}^{(L-1)} h_i \delta\left(\tau - \tau_i\right) \delta\left(\nu - \nu_i\right), \tag{3}$$

where L and h_i denote the number of channel paths and the channel gain at the $i-$th path, respectively, and $\delta(.)$ indicates the Dirac Delta function. Still referring to (3), the delay and the Doppler shifts τ_i and ν_i for the $i-$th path are given by $\tau_i = \frac{\ell_i}{M\triangle f}$ and $\nu_i = \frac{\kappa_i}{NT}$, respectively, where $\triangle f = \frac{1}{T}$, and ℓ_i and κ_i denote the delay and the Doppler indices, respectively.

Denoting the continuous time transmit signal by $s(t)$, the TD signal received at the $k-$th processing element of RIS can be written [13], [26], [58] as:

$$r_{SR,k}(t) = \int_{\nu}\int_{\tau} h_{SR,k}(\tau,\nu)s(t-\tau)e^{j2\pi\nu(t-\tau)}\mathrm{d}\tau\mathrm{d}\nu + w_{SR,k}(t), \quad (4)$$

where the suffix 'SR' refers to the source-to-RIS link, and $w_{SR,k}(t)$ denotes the TD additive white Gaussian noise (AWGN) corresponding to the source-to-the $k-$th processing element of RIS link.

To have a clear understanding of both the source-to-RIS and the RIS-to-destination channels and the input-output relationship in the DD and the TD, we now commence with the channel behavior. Specifically, the TD output over the doubly selective channels can be expressed in a simple matrix multiplication-based representation as

$$\boldsymbol{r}_{SR,k} = \boldsymbol{H}_{SR,k}\boldsymbol{s}, \quad (5)$$

where the channel transfer matrix can be expressed [23], [60] as:

$$\begin{aligned}\boldsymbol{H}_{SR,k} &= h_0\boldsymbol{P}^0\boldsymbol{\Lambda}_0 + h_1\boldsymbol{P}^1\boldsymbol{\Lambda}_1 + \cdots + h_{L-1}\boldsymbol{P}^{L-1}\boldsymbol{\Lambda}_{L-1} \\ &= \sum_{i=0}^{(L-1)} h_{SR,k,i}\boldsymbol{P}^i\boldsymbol{\Lambda}_i, \end{aligned} \quad (6)$$

where the $MN \times MN$ permutation matrix $\boldsymbol{P}$ is expressed [23], [60] as

$$\boldsymbol{P} = \begin{bmatrix} 0 & \dots & 0 & 1 \\ 1 & \dots & 0 & 0 \\ \vdots & \ddots & \vdots & \vdots \\ 0 & \dots & 1 & 0 \end{bmatrix}_{MN\times MN}, \quad (7)$$

the Doppler shift matrix $\boldsymbol{\Lambda}_i$ is given [23], [24], [60] by

$$\boldsymbol{\Lambda}_i = \begin{bmatrix} e^{\frac{j2\pi k_i(0)}{MN}} & 0 & \dots & 0 \\ 0 & e^{\frac{j2\pi k_i(1)}{MN}} & \dots & 0 \\ \vdots & & \ddots & \vdots \\ 0 & 0 & \dots & e^{\frac{j2\pi k_i(MN-1)}{MN}} \end{bmatrix}_{MN\times MN}, \quad (8)$$

and the channel gain corresponding to the $i-$th path is expressed as h_i.

Thus, the channel transfer matrix $\boldsymbol{H}_{SR,k}$ in (6) can be viewed as a combination of a circulant matrix characterizing the circular shifts in accordance with the channel delays, and the Doppler shift matrix $\boldsymbol{\Lambda}_i$ given by (8). Specifically,

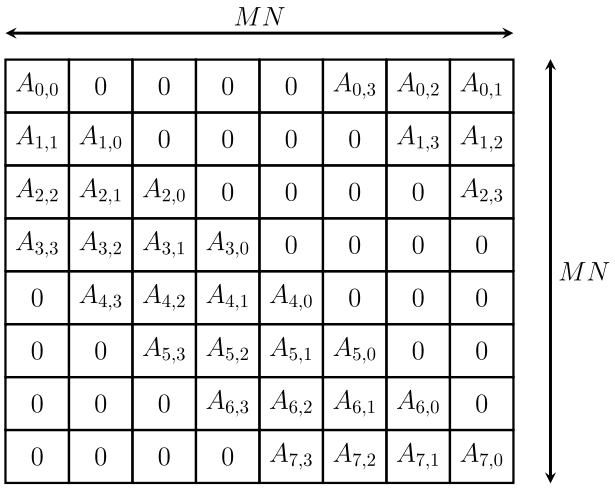

$A_{0,0}$	0	0	0	0	$A_{0,3}$	$A_{0,2}$	$A_{0,1}$
$A_{1,1}$	$A_{1,0}$	0	0	0	0	$A_{1,3}$	$A_{1,2}$
$A_{2,2}$	$A_{2,1}$	$A_{2,0}$	0	0	0	0	$A_{2,3}$
$A_{3,3}$	$A_{3,2}$	$A_{3,1}$	$A_{3,0}$	0	0	0	0
0	$A_{4,3}$	$A_{4,2}$	$A_{4,1}$	$A_{4,0}$	0	0	0
0	0	$A_{5,3}$	$A_{5,2}$	$A_{5,1}$	$A_{5,0}$	0	0
0	0	0	$A_{6,3}$	$A_{6,2}$	$A_{6,1}$	$A_{6,0}$	0
0	0	0	0	$A_{7,3}$	$A_{7,2}$	$A_{7,1}$	$A_{7,0}$

FIGURE 2. Typical shape of the time-domain channel transfer matrix of an OTFS channel.

the channel transfer matrix of a time-invariant frequency selective channel is circulant, and can be seen [7], [16], [17], [32] as:

$$\breve{\boldsymbol{H}} = \begin{bmatrix} h_0 & 0 & \cdots & h_{(L-1)} & \cdots & h_2 & h_1 \\ h_1 & h_0 & \cdots & & \cdots & h_3 & h_2 \\ \vdots & \vdots & \ddots & \ddots & \ddots & \ddots & \vdots \\ h_{(L-1)} & h_{(L-2)} & \cdots & h_0 & \ddots & 0 & 0 \\ \vdots & \vdots & \ddots & \ddots & \ddots & \ddots & \vdots \\ 0 & 0 & \cdots & h_{(L-2)} & \dots & h_0 & 0 \\ 0 & 0 & \cdots & h_{(L-1)} & \cdots & h_1 & h_0 \end{bmatrix}, \quad (9)$$

where the 'SR' suffix has been dropped for clarity.

The circulant matrix $\breve{\boldsymbol{H}}$ can be expressed as the sum of L matrices given [6], [24], [60] by

$$\begin{aligned}\breve{\boldsymbol{H}} &= h_0\boldsymbol{P}^0 + h_1\boldsymbol{P}^1 + h_2\boldsymbol{P}^2 + \cdots + h_{L-1}\boldsymbol{P}^{L-1} \\ &= \sum_{i=0}^{(L-1)} h_i\boldsymbol{P}^i. \end{aligned} \quad (10)$$

We see that the time-invariant frequency selective channel can be expressed by the circulant matrix $\breve{\boldsymbol{H}}$ in a form either as (9) or as (10). The incorporation of the Doppler shift matrix $\boldsymbol{\Lambda}_i$ of (8) with $\breve{\boldsymbol{H}}$ of (9) results in $\boldsymbol{H}_{SR,k}$ of (6) for characterizing a doubly selective channel.

The typical shape of the source-to-RIS channel $\boldsymbol{H}_{SR,k}$ or the RIS-to-destination channel $\boldsymbol{H}_{RD,k}$ is shown in Fig. 2. The shape is seen to be similar to the matrix $\breve{\boldsymbol{H}}$ of (9). However, due to the presence of Doppler-related diagonal components of $\boldsymbol{\Lambda}_i$, all the diagonal elements of $\boldsymbol{H}_{SR,k}$ are not equal except for the main diagonal. Hence, $\boldsymbol{H}_{SR,k}$ and $\boldsymbol{H}_{RD,k}$ are not, in general, circulant matrices.

C. RIS PROCESSING

The signal received at the RIS passes through a controlled propagation medium. Each processing element of RIS will

include its own phase shift with that of the OTFS modulated signal incident on it. A direct path between the transmitter and the receiver may or may not exist. When a direct path exists, the phase changes induced by all of the elements are summed coherently, resulting in a focused beam of the signal. Beamforming using RIS increases the signal reception scenario of the direct-path signal. For NLOS communications, the OTFS modulated signal impinges on the RIS and then to the target user, thereby covering blockage or a blind spot in the channel. We consider both the source-to-RIS and the RIS-to-destination links to be high-speed doubly selective channels with L channel paths, and as such, may be modeled in a similar way: $\boldsymbol{H}_{SR,k} = \sum_{i=0}^{(L-1)} h_{SR,k,i}\boldsymbol{P}^i\boldsymbol{\Lambda}_i$, and $\boldsymbol{H}_{RD,k} = \sum_{i=0}^{(L-1)} h_{RD,k,i}\boldsymbol{P}^i\boldsymbol{\Lambda}_i$, where the suffix 'RD' refers to the RIS-to-destination link. The transmitted signal impinges on the RIS at an arbitrary angle, and the RIS 'reconfigures' the phase shift by which the incident signal will be reflected toward the destination. Hypothetically, RIS can tune any phase shift using receiver feedback on near-instantaneous channel conditions to reflect the signal in the desired direction. Practically, the phase response of RIS is controlled by a controller and the associated software. An approach based on the ℓ_2- norm maximization of the effective channel matrix has been proposed in [55] for the design of the reflection phase shift. To outline the RIS processing, the received signal at the destination can be expressed as [61]:

$$\boldsymbol{r} = \sqrt{P_t}\left[\sqrt{P_L}\sum_{k=0}^{(K-1)}\boldsymbol{H}_{SR,k}e^{j(\boldsymbol{\phi}_k)}\boldsymbol{H}_{RD,k}\right]\boldsymbol{s} + \boldsymbol{W}, \quad (11)$$

where P_t indicates the transmit power, P_L represents the path loss, $\boldsymbol{W}$ denotes the additive white Gaussian noise (AWGN), and $\boldsymbol{\phi}_k$ represents the phase angle matrices of the corresponding elements of the RIS. Let us further represent the phase angle of the combined source to RIS's $k-$th element plus the element-to-destination link by $\boldsymbol{\theta}_k$.

For maximization of the channel SNR, we consider the phase shift by which the signal is reflected towards the receiver to be given by [61], [62], [63]:

$$\boldsymbol{\phi}_k = \boldsymbol{\theta}_k = \angle\left(\boldsymbol{H}_{SR,k}\boldsymbol{H}_{RD,k}\right), \quad (12)$$

where '$\angle\bullet$' refers to the phase angle matrix containing phases of the elements of the matrix'$\bullet$'. We consider the channel information corresponding to the source-to-RIS link and the RIS-to-destination link is available at the RIS. The overall channel response of our RIS-assisted DD channel is [34]:

$$\begin{aligned}\boldsymbol{H}_o &= \sum_{k=1}^{K}\left(\boldsymbol{H}_{SR,k}\boldsymbol{\Psi}_k\boldsymbol{H}_{RD,k}\right)\\ &= \sum_{k=1}^{K}\left(\boldsymbol{H}_{SR,k}e^{-j\boldsymbol{\phi}_k}\boldsymbol{H}_{RD,k}\right). \quad (13)\end{aligned}$$

Finally, the signal received at the receiver will be:

$$\boldsymbol{r} = \boldsymbol{H}_o\boldsymbol{s} + \boldsymbol{W}. \quad (14)$$

The elements of a RIS are typically sub-wavelength in size and the phase shift introduced usually depends on the size as well as the number of RIS elements [36]. Again, the accuracy with which a RIS can change the channel phase to the target user is a measure of its performance. Equation (12) is used to calculate the ideal phase shift introduced by a RIS in order to maximize the SNR. To justify (12), let us consider that $\boldsymbol{\Delta\Phi_k} = \boldsymbol{\phi_k} - \boldsymbol{\theta_k}$. Then the received signal at the destination can be written as [61], [62], [63]:

$$\boldsymbol{r} = \sqrt{P_t}\left[\sqrt{P_L}\sum_{k=0}^{(K-1)}\boldsymbol{H}_{SR,k}e^{j(\Delta\boldsymbol{\Phi}_k)}\boldsymbol{H}_{RD,k}\right]\boldsymbol{s} + \boldsymbol{W} \quad (15)$$

The SNR obtained from (15) is given by:

$$\gamma = \frac{\left|\sqrt{P_L}\sum_{k=0}^{(K-1)}\boldsymbol{H}_{SR,k}e^{j(\Delta\boldsymbol{\Phi}_k)}\boldsymbol{H}_{RD,k}\right|^2 P_t}{W}. \quad (16)$$

The SNR γ of (16) will be maximized, when

$$\begin{aligned}\Delta\boldsymbol{\Phi}_k &= \phi_k - \boldsymbol{\theta}_k = 0,\\ \text{i.e.,}\ \ \phi_k &= \boldsymbol{\theta}_k.\end{aligned}$$

Thus, for SNR maximization, the total phase shift introduced by the RIS elements should be equal to the phase angle of the combined source to RIS's $k-$th element plus the element-to-destination link.

D. RECEIVER PROCESSING: OTFS DEMODULATION AND DETECTION

At the receiver end, the TD received signal is first converted into the DD domain using OTFS demodulation, and then the DD signal is detected using different conventional detectors or the proposed DL-based detector. For OTFS demodulation, at first, the Wigner transform is used to convert the TD signal to the TF domain. Then the symplectic fast Fourier transform (SFFT) is used to convert the TF domain signal to the DD domain. The OTFS demodulation is discussed in Section II-E and the shapes of the channel transfer matrices in different domains are elaborated in Section II-F. The conventional detectors are then highlighted in Section II-G.

E. OTFS DEMODULATION

The received TD signal $\boldsymbol{r}$ is de-vectorized to the $M \times N$ TF matrix denoted by $\boldsymbol{R} = \text{vec}^{-1}(\boldsymbol{r})$. Thus, the Wigner transform performs the reverse operation of the Heisenberg transform. It maps back the received time domain signal to TF domain. The symplectic Fourier transform (SFFT) is finally performed on $\boldsymbol{R}$ to convert the TF domain signal to the DD domain. This is accomplished by an $M-$point FFT followed by the SFFT operation. The demodulated DD domain signal,

$$\boldsymbol{H}_{\text{eff}}^{\text{OTFS}} = \left[\begin{array}{cccc:cccc:cccc:cccc} a_0 & 0 & 0 & 0 & 0 & 0 & 0 & 0 & 0 & 0 & 0 & 0 & 0 & 0 & 0 & c_0 \\ 0 & a_0 & 0 & 0 & 0 & 0 & 0 & 0 & 0 & 0 & 0 & 0 & b_9 & 0 & 0 & 0 \\ 0 & 0 & a_0 & 0 & 0 & 0 & 0 & 0 & 0 & 0 & 0 & 0 & 0 & b_{10} & 0 & 0 \\ 0 & 0 & 0 & a_0 & 0 & 0 & 0 & 0 & 0 & 0 & 0 & 0 & 0 & 0 & b_{11} & 0 \\ \hdashline 0 & 0 & 0 & c_3 & a_0 & 0 & 0 & 0 & 0 & 0 & 0 & 0 & 0 & 0 & 0 & 0 \\ b_0 & 0 & 0 & 0 & 0 & a_0 & 0 & 0 & 0 & 0 & 0 & 0 & 0 & 0 & 0 & 0 \\ 0 & b_1 & 0 & 0 & 0 & 0 & a_0 & 0 & 0 & 0 & 0 & 0 & 0 & 0 & 0 & 0 \\ 0 & 0 & b_2 & 0 & 0 & 0 & 0 & a_0 & 0 & 0 & 0 & 0 & 0 & 0 & 0 & 0 \\ \hdashline 0 & 0 & 0 & 0 & 0 & 0 & 0 & c_2 & a_0 & 0 & 0 & 0 & 0 & 0 & 0 & 0 \\ 0 & 0 & 0 & 0 & b_3 & 0 & 0 & 0 & 0 & a_0 & 0 & 0 & 0 & 0 & 0 & 0 \\ 0 & 0 & 0 & 0 & 0 & b_4 & 0 & 0 & 0 & 0 & a_0 & 0 & 0 & 0 & 0 & 0 \\ 0 & 0 & 0 & 0 & 0 & 0 & b_5 & 0 & 0 & 0 & 0 & a_0 & 0 & 0 & 0 & 0 \\ \hdashline 0 & 0 & 0 & 0 & 0 & 0 & 0 & 0 & 0 & 0 & 0 & c_1 & a_0 & 0 & 0 & 0 \\ 0 & 0 & 0 & 0 & 0 & 0 & 0 & 0 & b_6 & 0 & 0 & 0 & 0 & a_0 & 0 & 0 \\ 0 & 0 & 0 & 0 & 0 & 0 & 0 & 0 & 0 & b_7 & 0 & 0 & 0 & 0 & a_0 & 0 \\ 0 & 0 & 0 & 0 & 0 & 0 & 0 & 0 & 0 & 0 & b_8 & 0 & 0 & 0 & 0 & a_0 \end{array}\right] \tag{17}$$

assuming rectangular pulse shaping, can be expressed [23], [25], [60] as:

$$\boldsymbol{Y} = \boldsymbol{F}_M^H \left(\boldsymbol{F}_M \boldsymbol{R}\right) \boldsymbol{F}_N^H. \tag{18}$$

Upon substitution of (2) in (14), the vectorially stacked form of the received DD grid can be expressed by [25], [60]:

$$\begin{aligned} \boldsymbol{y} &= \left(\boldsymbol{F}_N \otimes I_M\right) \boldsymbol{r}. \\ &= \left(\boldsymbol{F}_N \otimes I_M\right) \left(\boldsymbol{H}_o \boldsymbol{s} + \boldsymbol{W}\right) \\ &= \left(\boldsymbol{F}_N \otimes I_M\right) \boldsymbol{H}_o \left(\boldsymbol{F}_N^H \otimes I_M\right) \boldsymbol{x} + \left(\boldsymbol{F}_N^H \otimes I_M\right) \boldsymbol{W} \\ &= \boldsymbol{H}_{\text{eff}} \boldsymbol{x} + \tilde{\boldsymbol{W}}, \end{aligned} \tag{19}$$

where $\tilde{\boldsymbol{W}} = \left(\boldsymbol{F}_N^H \otimes I_M\right) \boldsymbol{W}$ indicates the DD domain AWGN and $\boldsymbol{H}_{\text{eff}}$ is the effective channel matrix given by $\boldsymbol{H}_{\text{eff}} = \left(\boldsymbol{F}_N \otimes I_M\right) \boldsymbol{H}_o \left(\boldsymbol{F}_N^H \otimes I_M\right)$.

F. SHAPES OF THE CHANNEL MATRICES IN DIFFERENT DOMAINS

For a clear understanding of the input-output relationship of the RIS-aided OTFS system and to design an appropriate detector, we need to know the shapes of the channel matrices in both the TD and the DD domains. Although the TD channel matrix for an OTFS system without RIS has the shape of a circulant matrix, it is not truly circulant due to the unequal diagonal elements caused by the Doppler matrix $\boldsymbol{\Lambda} i$ in $\boldsymbol{H}_{SR,k}$ of (6). However, the TD channel matrix for the RIS-OTFS system, expressed by equation (13), is circulant. Because the RIS-induced phase shift and the multiplication of similar components of the channel matrices provide real-valued elements in (13). The matrix shape is similar to the TD OTFS channel matrix shown in Fig. 2. Since the diagonal elements are converted back to equal values, the TD RIS-OTFS channel matrix is circulant, as shown in Fig. 3.

The previous literature, including [24], [54], [60], [64], discussed the DD channel of OTFS and RIS-aided OTFS. However, a more comprehensive discussion on the actual shape of the DD channel is still necessary. The mathematical

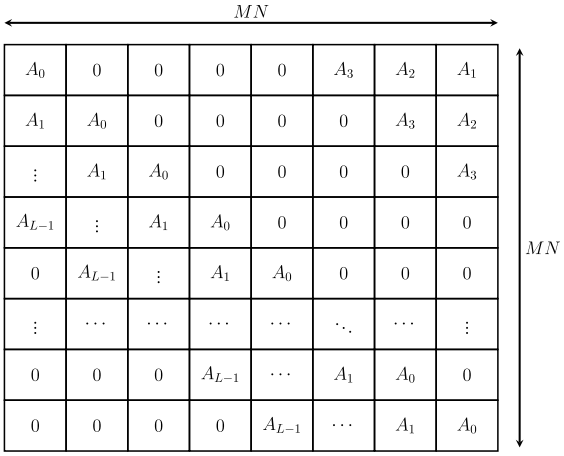

FIGURE 3. Typical shape of the time-domain channel transfer matrix of RIS-assisted OTFS channel.

derivation of the TD channel can be found in [24], [53], and [60]. Here, rather than providing the details of these derivations, we provide a simple discussion on the shapes of the DD domain channel matrix.

To discuss the DD channel matrix of an OTFS system, let us consider an example with $M = 4$, $N = 4$, and $L = 2$. The shape of the TD channel matrix is similar to the one shown in Fig. 2 and can be represented as:

$$\breve{\boldsymbol{H}}_{TD} = \begin{bmatrix} A_0 & 0 & \cdots & 0 & C_1 \\ B_0 & A_1 & \cdots & 0 & 0 \\ 0 & B_1 & \cdots & 0 & 0 \\ \vdots & \vdots & \ddots & \ddots & \vdots \\ 0 & 0 & \cdots & B_{14} & A_{15} \end{bmatrix}. \tag{20}$$

To obtain the DD channel, we use the following equation: $\boldsymbol{H}_{\text{eff}}^{\text{OTFS}} = \left(\boldsymbol{F}_N \otimes I_M\right) \breve{\boldsymbol{H}}_{TD} \left(\boldsymbol{F}_N^H \otimes I_M\right)$ mentioned in Subsection II-E. The result is illustrated in (17), as shown at the top of the page, which represents the typical shape of the DD channel without the assistance of RIS. In (17), we notice that the DFT-based eigendecomposition and the Kronecker

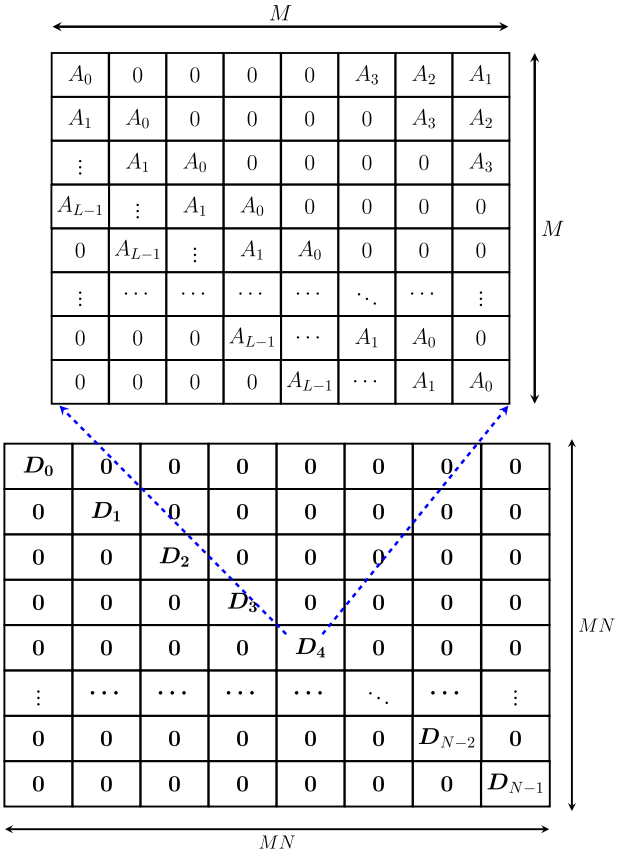

FIGURE 4. Typical shape of the DD channel transfer matrix for RIS-assisted OTFS. We see that this is block diagonal matrix, where each of the diagonal submatrices is circulant.

product have rendered the DD channel matrix a specific shape. The DD channel matrix $\boldsymbol{H}_{\text{eff}}^{\text{OTFS}}$ shown in (17) has components $a_0, a_1, \cdots, a_{15}$ along the main diagonal, which correspond to $A_0, A_1, \cdots, A_{15}$ of (20). However, the other diagonal components $b_0, b_1, \cdots, b_{11}$ and $c_0, c_1, \cdots, c_3$ are shifted and dispersed across the $M \times M$ submatrices.

By contrast, the DD channel matrix of a RIS-aided OTFS system can be obtained from its TD counterpart, which is expressed by $\boldsymbol{H}o$ in Equation (14). To obtain the corresponding DD channel matrix, we can use the same equation: $\boldsymbol{H}_{\text{eff}}^{\text{RIS-OTFS}} = (\boldsymbol{F}_N \otimes I_M)\,\boldsymbol{H}_o\,(\boldsymbol{F}_N^H \otimes I_M)$. As discussed earlier and shown in Fig. 3, $\boldsymbol{H}_o$ is a real circulant matrix. Therefore, $\boldsymbol{H}_{\text{eff}}^{\text{RIS-OTFS}}$ is a block diagonal matrix, with each diagonal submatrix being circulant. The off-diagonal submatrices of $\boldsymbol{H}_{\text{eff}}^{\text{RIS-OTFS}}$ are transformed into zero matrices, $\mathbf{0}_{M\times M}$, by the phase adjustment performed by the RIS. Thus RIS can favorably redirect the signal, thereby increasing the directivity of transmission. The typical shape of $\boldsymbol{H}_{\text{eff}}^{\text{RIS-OTFS}}$ is illustrated in Figure 4, where the diagonal submatrices are shown above the main block diagonal matrix. To provide a better visual, Table 1 summarizes the shape of the CSI matrices in different domains.

Above all, the $MN \times MN$ channel transfer matrix - which can be either in the TD or in the DD domain for the OTFS system with or without RIS - has a total number of L non-zero terms in each row or in each column. Thus the matrix is a sparse matrix, which facilitates a low-complexity channel estimation, and a low-complexity detector can be employed.

TABLE 1. Shape of the CSI matrices in different domains.

Domain	OTFS	RIS-OTFS
Time	Non-circulant matrix	Circulant matrix
Delay-Doppler	Block matrix	Block-diagonal matrix
Equation used: $\boldsymbol{H}_{\text{DD}} = (\boldsymbol{F}_N \otimes I_M)\,\boldsymbol{H}_t\left(\boldsymbol{F}_N^H \otimes I_M\right)$		

G. CONVENTIONAL DETECTORS

For the detection, linear zero-forcing (ZF) and minimum mean square error (MMSE) detectors can be employed. As a non-linear detector candidate, the message passing algorithm (MPA) based detector can also be considered.

1) LINEAR DETECTORS

Linear detectors are filters that reverse the channel effects on the received signal. Using the simplified matrix multiplication-based DD domain relationship of (19), the DD grids may be detected with the aid of zero-forcing (ZF) detectors:

$$\hat{\boldsymbol{x}}_{\text{ZF}} = \left(\boldsymbol{H}_{\text{eff}}^H \boldsymbol{H}_{\text{eff}}\right)^{-1} \boldsymbol{H}_{\text{eff}}^H \boldsymbol{y}. \tag{21}$$

To mitigate the performance degradation due to ZF-induced noise enhancement, minimum mean-squared error (MMSE) detector may also be employed:

$$\hat{\boldsymbol{x}}_{\text{MMSE}} = \left(\boldsymbol{H}_{\text{eff}}^H \boldsymbol{H}_{\text{eff}} + \sigma_N^2 I_{MN}\right)^{-1} \boldsymbol{H}_{\text{eff}}^H \boldsymbol{y}, \tag{22}$$

where σ_N^2 denotes the noise variance. We note that these linear detectors have a computational complexity of $\mathcal{O}(M^3N^3)$ [65], [66], as they require inversion of $MN \times MN$ matrices.

2) MESSAGE PASSING DETECTOR

Message passing algorithm (MPA) can be effectively applied to recover the RIS-aided OTFS signal. As seen from (19), $\boldsymbol{H}_{\text{eff}}$ is a sparse matrix, and hence MPA-based detector may be employed using $\boldsymbol{y}$ as the observation nodes and $\boldsymbol{x}$ as the variable nodes. The detector recovers the transmitted signal passing variance and the mean of interference between variable nodes and observation nodes.

Denoting r' and c as the number of rows and columns of the $\boldsymbol{H}_{\text{eff}}$, respectively, $\mathcal{I}(r')$ and $\mathcal{J}(c)$ as the set of indices of non-zero elements of $\boldsymbol{H}_{\text{eff}}$. $\boldsymbol{p}_{c,r'}$ as the probability mass function (pmf) for message passing from variable nodes to observation node, the mean $\mu_{r',c}^{(a)}$ and the variance $\left(\sigma_{r',c}^{(a)}\right)^2$ at the $a-$th iteration can be calculated for observation nodes by [27], [67]:

$$\mu_{r',c}^{(a)} = \sum_{e\in\mathcal{I}(r), e\neq c} \sum_{j=1}^{\mathcal{L}} p_{e,r'}^{(i-1)}\left(a_j\right) a_j H_{\text{eff}}[r', e], \tag{23}$$

and

$$\left(\sigma_{r',c}^{(a)}\right)^2 = \sum_{e\in\mathcal{I}(r'),e\neq c}\left(\sum_{j=1}^{\mathcal{L}} p_{e,r'}^{(a-1)}(s)\left|s_j\right|^2\left|H_{\text{eff}}[r',e]\right|^2 v - \left|\sum_{j=1}^{\mathcal{L}} p_{e,r'}^{(a-1)}(s_j)\, s_j H_{\text{eff}}[r',e]\right|^2\right) + \sigma^2, \tag{24}$$

respectively, where σ^2 denotes the noise power.

The variable nodes update the vector $\boldsymbol{p}_{c,r'}^{(a)}$ using (25) [23], [27]:

$$p_{c,r'}^{(a)}(s_j) = \Delta\cdot\tilde{p}_{c,r'}^{(a)}(s_j) + (1-\Delta)\cdot p_{c,r'}^{(a-1)}(s_j),\ s_j\in\mathbb{A} \tag{25}$$

where $\mathbb{A}$ denotes the modulation alphabet and Δ is the damping factor. Then, we have [23], [67]:

$$\begin{aligned}\tilde{p}_{c,r'}^{(a)}(s_j) &\propto \prod_{e\in\mathcal{J}(c),e\neq r'}\Pr\left(y[e]\mid x[c]=s_j, H_{\text{eff}}\right)\\ &= \prod_{e\in\mathcal{J}(c),e\neq r'}\frac{\xi^{(a)}(e,c,j)}{\sum_{k=1}^{\mathcal{L}}\xi^{(a)}(e,c,k)}\end{aligned} \tag{26}$$

where

$$\xi^{(a)}(e,c,k) = \exp\left(\frac{-\left|\boldsymbol{y}[e]-\mu_{e,c}^{(a)}-\boldsymbol{H}_{e,c}\boldsymbol{s}_k\right|^2}{\left(\sigma_{e,c}^{(a)}\right)^2}\right) \tag{27}$$

This transfer of variance and mean is performed in two steps.

- In the first step, the Gaussian distributed variance $\left(\sigma_{r',c}^{(a)}\right)^2$ and the mean $\mu_{r',c}^{(a)}$ of $\zeta_{r',c}^{(a)}$ is computed by the observation nodes $\boldsymbol{y}[r']$ using $\boldsymbol{p}_{c,r'}^{(a-1)}$. Then the observation node passes the $\left(\sigma_{r',c}^{(a)}\right)^2$, $\mu_{r',c}^{(a)}$ and $\boldsymbol{p}_{c,r'}^{(a-1)}$ to variable nodes $\boldsymbol{x}[c]$, $c\in\mathcal{I}(r')$
- In the second step, the $\boldsymbol{p}_{c,r'}^{(a)}$ is updated by the variable nodes by using $\left(\sigma_{r',c}^{(a)}\right)^2$, $\mu_{r',c}^{(a)}$ and $\boldsymbol{p}_{c,r'}^{(a-1)}$. Then the variable nodes pass the $\boldsymbol{p}_{c,r'}^{(a)}$ to the observation nodes $\boldsymbol{y}[r']$, $r\in\mathcal{J}(c)$.

This process will be continued until a satisfactory criterion is reached. The MPA-based detectors have low complexity due to their graph-based approach, message-passing-based operation, and use of soft decision metrics. The complexity of MPA-based detectors is given by $\mathcal{O}(n_{iter}NMS\mathcal{L})$ [23], [68]. Because, as in obtaining (26), we first compute:

$$p_c^{(i)}(a_j) = \prod_{e\in\mathcal{J}(c)}\frac{\xi^{(i)}(e,c,j)}{\sum_{k=1}^{\mathcal{L}}\xi^{(i)}(e,c,k)}$$

which has a complexity of $O(NM\mathcal{L})$, and then we divide $p_c^{(i)}(a_j)$ by the term related to $e = r'$ for all r', which has complexity of $O(S)$ for each c. Hence, the overall complexity for a single iteration becomes $O(NMS\mathcal{L})$, where $S = \left|\mathcal{I}_r'\right| = |\mathcal{J}_c|$. Therefore for n_{iter} iteration, the complexity is $\mathcal{O}(n_{iter}NMS\mathcal{L})$, which is much lower than linear detectors of Section II-G1.

III. PROPOSED DEEP LEARNING-BASED DETECTOR

Deep learning (DL)-based detectors have become increasingly popular in wireless communication due to their ability to handle complex and non-linear systems, and to efficiently process a large volume of data. In this section, we propose a DL-based detector for the RIS-aided OTFS system. The DL-based detector is composed of three steps - data collection, training, and testing [69], [70], [71]. A new approach to dataset generation, training, and testing is considered for the signal detection of the system considered.

DL uses forward propagation as well as backpropagation and works with the aid of an activation function and an appropriate optimization technique. In a typical feedforward neural network, each neuron in a layer receives inputs from the previous layer, performs a weighted sum of these inputs, and applies an activation function to produce an output. The output of a neuron j in layer l can be computed by adding up the weighted inputs from the previous layer, adding a bias term, and applying an activation function [69], [72]:

$$z_j^l = \sum_{i=1}^{n_{l-1}} w_{ji}^l a_i^{l-1} + b_j^l \quad a_j^l = f(z_j^l) \tag{28}$$

where w_{ji}^l denotes the weight of the connection between neuron i in layer $l-1$ and neuron j in layer l, a_i^{l-1} the output of neuron i in layer $l-1$, b_j^l the bias term for neuron j in layer l, n_{l-1} the number of neurons in layer $l-1$, and f indicates the activation function applied to the weighted sum of inputs. The activation function decides whether the information received by the neuron is significant or not. In this work, SELU (Scaled Exponential Linear Unit) activation function is used as it very often outperforms other activation functions [73] and is defined by [73], [74]:

$$f(x) = \begin{cases}\lambda x, & x>0\\ \lambda\alpha\left(e^x-1\right), & x\leq 0\end{cases} \tag{29}$$

where α and λ are pre-defined constants ($\alpha = 1.67326324$, and $\lambda = 1.05070098$).

In the backpropagation process, the weights and biases are first randomly set - then the weights and biases are updated after each epoch of forward propagation based on the loss function or the difference between the output of that epoch and the ground truth. Since we consider the signal detection as a classification problem, we use the categorical cross-entropy loss function, which is defined by [70], [75]:

$$\mathrm{C} = -\sum_{j=1}^{\ddot{c}}\ddot{y}_j\log\left(\hat{y}_j\right) \tag{30}$$

where, $\ddot{y}$, $\hat{y}$, and $\ddot{c}$ denote the actual value, the predicted value, and the number of classes, respectively.

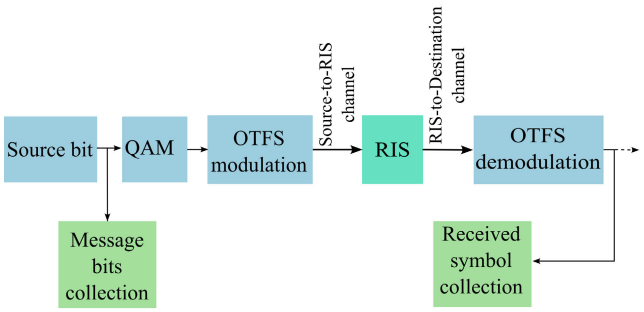

FIGURE 5. Data collection process of the DL-based detector for the RIS-aided OTFS scheme.

The gradient of the loss function with respect to the weights and biases of the network can be computed recursively using the chain rule [71], [76]:

$$\frac{\partial C}{\partial w_{ji}^{l}} = a_i^{l-1}\delta_j^l \quad \frac{\partial C}{\partial b_j^{l}} = \delta_j^l \tag{31}$$

where δ_j^l indicates the gradient of the loss function with respect to the output of neuron j in layer l and is computed by [74], [76]: $\delta_j^l = \frac{\partial C}{\partial a_j^l} \odot f'(z_j^l)$, where f' is the derivative of the activation function. The backpropagation followed by forward propagation will be continued until the minimum loss point or a satisfactory criterion is reached. The minimum point is generally found using the stochastic gradient descent (SGD) method. SGD updates the weights and biases of the network in the direction of the negative gradient of the loss function, scaled by a learning rate [77], [78]:

$$w_{ji}^{l} \leftarrow w_{ji}^{l} - \eta \frac{\partial C}{\partial w_{ji}^{l}} \tag{32}$$

$$b_{j}^{l} \leftarrow b_{j}^{l} - \eta \frac{\partial C}{\partial b_{j}^{l}} \tag{33}$$

where η denotes the learning rate.

Let us now elaborate on the proposed DL-based detector for the RIS-aided OTFS system.

1) DATA COLLECTION

In this step, the pseudo-randomly generated transmit message bits and the received symbols after OTFS demodulation are collected [72], [79]. Fig. 5 depicts the data collection process more clearly.

As shown in Fig. 5, the message bits are pseudo-randomly generated, and collected as 'transmit bits'. The received symbols corresponding to the transmitted bits are also collected after OTFS demodulation and are referred to as the 'received symbols'. Each frame of transmit bits forms a DD grid and the corresponding demodulated received symbols are arranged row-wise to form the dataset. Thus the number of samples in the generated dataset is equal to the number of transmitted frames. For example, if 5000 frames are transmitted, the dataset will contain 5000 samples. For the detection problem, the received symbols are considered as 'features', and the transmit bits are the 'targets'. Present DL models do not support complex numbers [80], [81], [82]. So, we store the real and imaginary parts of the received symbols separately in the dataset [64], [83], [84]. As a result, the dataset contains $2MN$ number of features. The structure of the collected dataset is shown in Fig. 6, where the data samples are shown across rows and the features are across the columns.

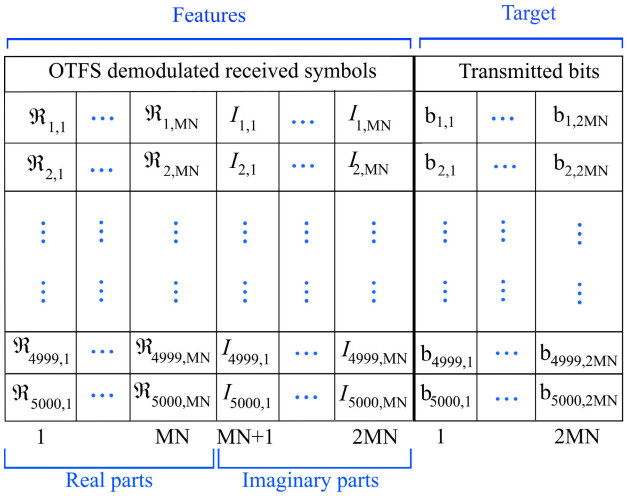

FIGURE 6. The structure of the collected dataset.

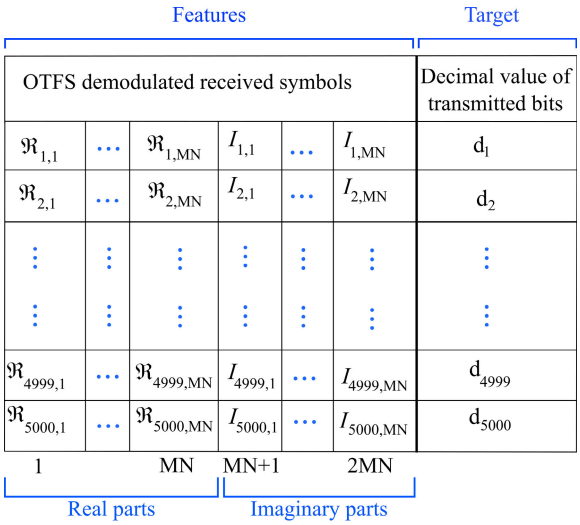

FIGURE 7. The structure of the converted dataset.

2) TRAINING

We note that the transmit bits are communicated over the RIS-aided OTFS scheme to generate the received symbols. The detector detects the source bits from the symbols received. As such, we train the model with the aid of a dataset generated for a specific SNR value [85], [86].

We convert the 'target' of the dataset from binary to the corresponding decimal values in order to create an optimum dataset for effectively employing DL for detection. Fig. 7 shows the structure of the converted dataset, where the

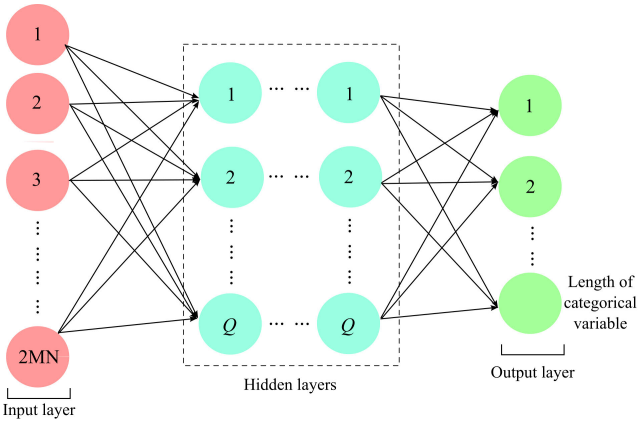

FIGURE 8. The DNN structure of the proposed DL-based deector.

TABLE 2. DNN parameters.

Parameters	Value
The activation function of the hidden layer	SELU
The activation function of the output layer	Softmax
Optimization function	Adam
Loss function	Categorical cross entropy
Number of training samples	5, 000
Number of neurons in each hidden layer, Q	128
Training SNR	0/10 dB
Number of epochs	300

transmitted bits of Fig. 6 have been replaced by their decimal values for facilitating the employment of our DL detector.

A fully connected deep neural network (DNN) is developed using the 'Keras' framework [87], [88]. Firstly, the decimal target values are converted into a categorical variable using the 'to_categorical' function from the Keras utility package. The network consists of three layers: one input, one output, and multiple hidden layers. The number of neurons in the input layer is $2MN$ and for the output layer, the number of neurons is similar to the length of categorical variables. In each of the hidden layers, there are Q neurons. The structure of the network is shown in Fig. 8. During the training, the validation split must be kept at 0 as all the members in the target variable are individual classes. For testing purposes, datasets generated for other SNRs may be used. The additional parameters of the model are given in Table 2 [54], [64], [89].

3) TESTING

The models trained at several SNR values are tested for a wide range of SNR. For testing purposes, the datasets are generated as described in Section. III-1. The preprocessing of the dataset is similar to that of the training step. Then the feature sets of the dataset are fed to the model to predict the category and the categorical variables are reconverted into the corresponding decimal classes. Finally, using a decimal-to-binary conversion, the predicted binary transmitted bits are achieved. During this conversion, the 0s from MSB bits of the frames (if any) might get missed. To handle this, the required number of zeros must be appended at the start of such frames. The flow chart of the testing algorithm is depicted in Fig. 9.

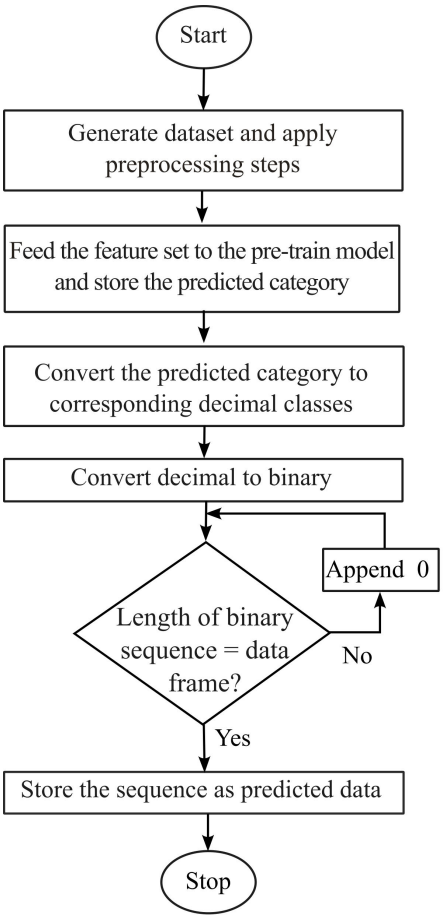

FIGURE 9. The flowchart of testing algorithm.

IV. COMPLEXITY IMPOSED BY THE DETECTORS

Here, we investigate the complexity imposed by the proposed DL-based detector and compare it with that imposed by conventional detectors. When the DNN is trained offline, computational complexity is not a significant concern since the time requirements are relatively low [90]. The complexity of the fully connected layer is calculated as $\mathcal{O}(\sum_{i=1}^{I} C_{i-1}C_i)$ [89], [91], where C_{i-1} and C_i represent the number of neurons in the previous layer and the current layer, respectively, and I indicates the total number of layers in the DNN structure. As a result, the complexity of the proposed DNN is $\mathcal{O}(\sum_{i=1}^{I-1} C_{i-1}C_i)$. The asymptotic complexity of the DNN is comparable to $\mathcal{O}(M^2N^2)$ [89]. By contrast, traditional

TABLE 3. Asymptotic complexity of the detectors used.

Detector	Complexity	Ref.
ZF	$\mathcal{O}(M^3N^3)$	[65], [66]
MMSE	$\mathcal{O}(M^3N^3)$	[65], [66]
MPA-Based	$\mathcal{O}\left(n_{iter}NMS\mathcal{L}\right)$	[44], [68]
DL-Based	$\mathcal{O}(M^2N^2)$	[90], [92]

detectors such as MMSE and ZF impose complexity of the order of $(MN)^3$ due to the matrix inversion operation, as already discussed in Section II-G1. Consequently, the computational complexity imposed by the DL-based detector is lower than that of MMSE and ZF linear detectors.

Table 3 summarizes the asymptotic complexities of the detectors used.

V. RESULTS AND DISCUSSION

In this section, we investigate the bit-error-rate (BER) performance of the RIS-aided OTFS system using ZF, MMSE, and MPA detectors. We have used 4-QAM modulation for mapping the source bits to symbols, and we have used a frame size of 10000. We have used an 8×8 DD grid. We use 4-tap channels for our investigations. The network parameters of the DNN model are given in Table 2. For controllable propagation, 16-element and 32-element RIS were considered. In addition to the conventional detection algorithms, we investigated the system's performance using the proposed DL-based detector. The results corresponding to the conventional detectors are discussed in subsection V-A, while that of the DL-based detector is presented in subsection V-B.

A. BER PERFORMANCE OF RIS-OTFS USING CONVENTIONAL DETECTORS

The performance of the RIS-assisted OTFS system using the conventional detectors mentioned in Subsection II-G is detailed here. We compared the BER of the RIS-aided OTFS and OTFS without RIS systems. We considered a doubly selective channel having Rayleigh distribution with 4 channel taps aggravated by Doppler spread. The error performance with ZF, MMSE, and MPA detectors is studied.

1) BER PERFORMANCE USING ZF DETECTOR

In Fig. 10, the suggested RIS-OTFS scheme's BER performance is shown using the ZF detector, and its performance is compared with that of an OTFS scheme without RIS. The ZF detector can deliver respectable performance for RIS-aided OTFS despite being a relatively basic detector with a straightforward design. We can see from Fig. 10 that a 16-element RIS greatly improves system performance when compared to an OTFS system without RIS. Additionally, we observe that the system offers a further decreased BER when outfitted with a RIS that has 32 processing elements. Thus, it is clear that the OTFS with a ZF detector can perform better in NLOS communication when supported by a RIS.

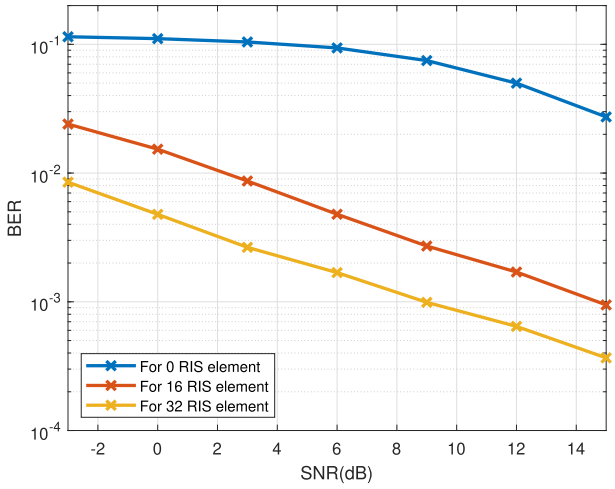

FIGURE 10. BER Performance of the ZF detector.

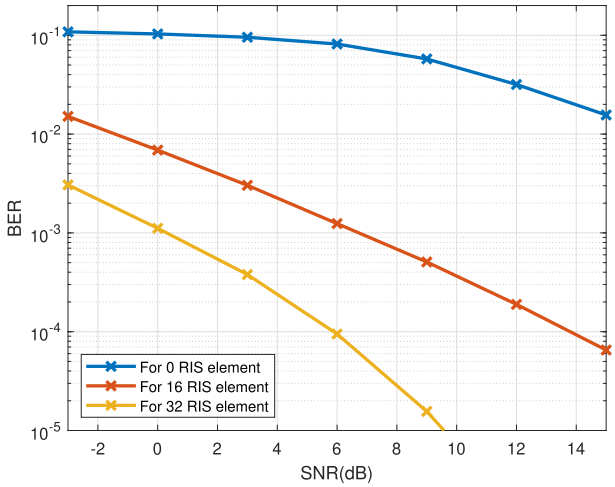

FIGURE 11. Performance analysis using MMSE detector.

2) BER PERFORMANCE USING MMSE DETECTOR

The BER performance of the RIS-OTFS system using an MMSE detector is shown in Fig. 11. It can be seen from Fig. 11 that the performance of the MMSE detector is superior to that of the ZF-based system. Similar to the ZF detector, using the MMSE detector also, the RIS-assisted OTFS system's performance is better than an OTFS system without RIS. We additionally note that, as was the case with the ZF detector, even with the MMSE detector, the performance of the RIS-OTFS system is enhanced by increasing the number of processing elements of RIS.

The performance will be even better if binary phase shift keying (BPSK) rather than QAM is used, as found by [53]. Fig.17 compares the performance of the proposed RIS-OTFS system for BPSK and 4-QAM modulation, using an MMSE detector. From Fig.17, it is proved that the detection is easier at lower modulation orders, for all 16 and 32 RIS elements.

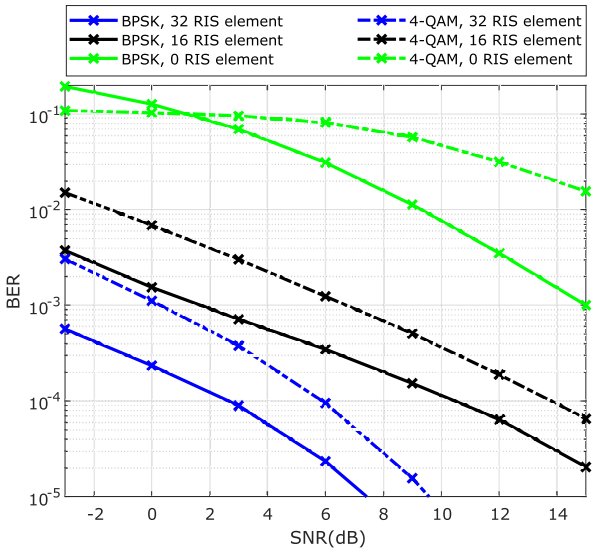

FIGURE 12. Performance comparison between BPSK and QAM using MMSE detector.

3) BER PERFORMANCE USING MPA DETECTOR

The MPA-based detector is widely used in OTFS receivers for their low-complexity design due to the sparse DD channel. Fig. 13 shows the BER performance of the RIS-aided OTFS system for both the 16 and 32 RIS processing elements. We observe from Fig. 13 that MPA-based OTFS system without RIS is subjected to extremely high erroneous detection in lower SNR values. On the other hand, RIS-implemented OTFS systems experience less performance degradation even in the highly dispersive channels. Introducing 16-element RIS significantly improves the performance of OTFS. The improved performance of the RIS-aided OTFS is attained due to RIS's capability to reduce ISI and to adaptively modify the phase shift of the OTFS signal. The BER reduces far more if the number of RIS elements is increased. Thus it can be inferred that the RIS-assisted system enhances the signal reception scenario using an MPA-based detector.

4) PERFORMANCE COMPARISON FOR DIFFERENT NUMBERS OF CHANNEL TAPS

Here, we investigate the impact of different numbers of channel taps on the performance of a RIS-assisted OTFS system. Channel taps represent the discrete delays and Doppler shifts in the time-domain channel impulse response. To investigate the impact of channel taps on the system's performance, we evaluated the system's BER performance using an MMSE detector using channels of 4, 6, and 8 taps in our simulation. Fig. 14 shows that the optimal number of taps depends on the SNR of the communication channel. At lower SNRs, using a higher number of taps, such as 6 taps, can provide improved performance. This is likely due to the additional taps being able to capture more details of the channel's time and frequency response, leading to better utilization of the available resources. On the other hand, the system performs better

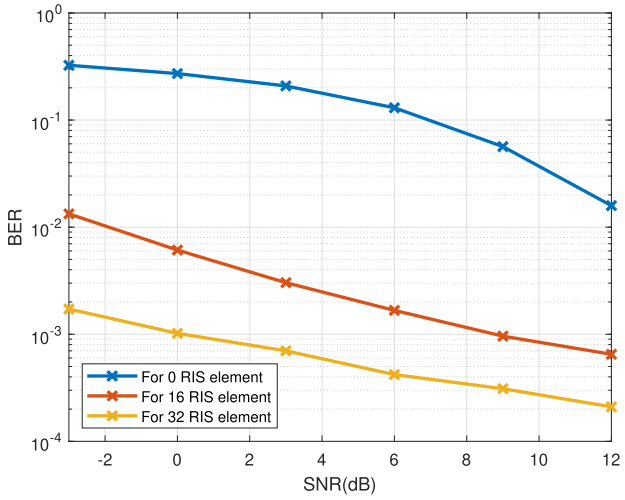

FIGURE 13. BER performance of the MPA-based detector.

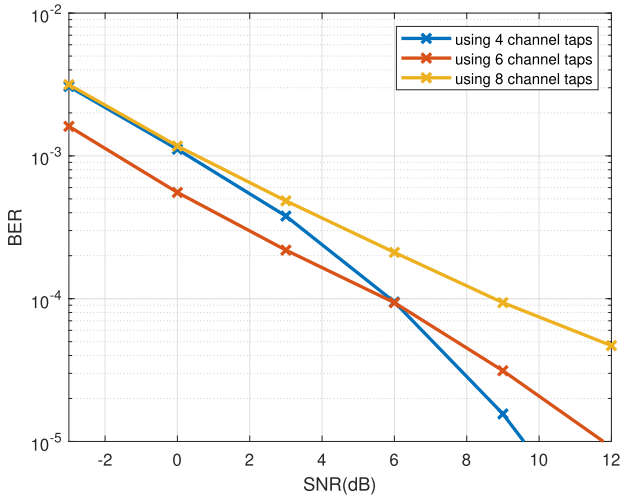

FIGURE 14. Variation of BER performance for different numbers of channel taps, using 32 RIS elements.

at higher SNRs for channels with a lower number of taps. This may be due to the fact that at higher SNRs, the signal power is sufficiently higher, thus the signal detection is easier. However, more taps introduce more noise and interference into the system, which can degrade the BER performance. Interestingly, we found that the channel of 8 taps did not improve the system's performance, regardless of the SNR. This suggests that there is a point of diminishing returns beyond which the error performance degrades.

B. BER PERFORMANCE OF THE PROPOSED DL-BASED DETECTOR

In this section, the performance of the DL-based detector for a RIS-aided OTFS system is discussed for different training SNR values. As described, the DL model can be trained with a dataset created for any training SNR - however, the training SNR should be within the operating SNR range. The error

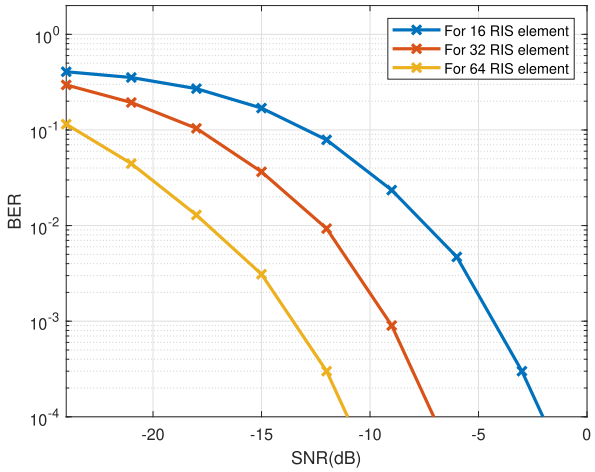

FIGURE 15. Error performance of DL-based detector trained at 10 dB.

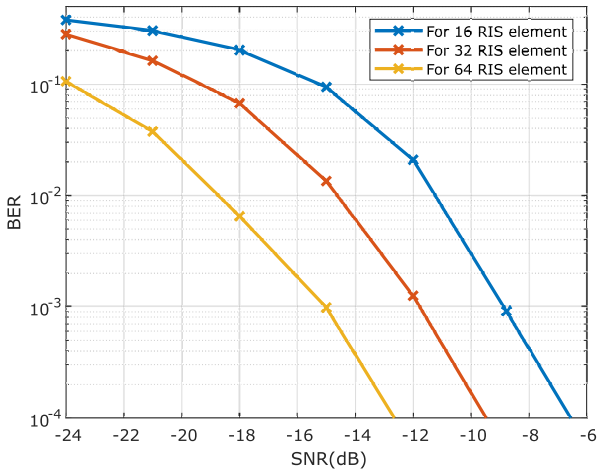

FIGURE 16. Error performance of DL-based detector trained at 0 dB.

performance of our DL-based detector is now discussed for training SNRs of 0 dB and 10 dB.

1) PERFORMANCE OF DL DETECTOR TRAINED AT 10 dB

Fig. 15 depicts the performance of the proposed DL-based detector for the RIS-OTFS for a training SNR of 10 dB. We considered the number of RIS elements to be 64, 32, and 16. As expected, the higher the number of RIS elements, the lower the BER. The DL-based detector with a training SNR of 10 dB and with a 64-element RIS can provide infinitesimally low BER at an SNR as low as -9 dB. When the number of RIS elements is decreased to 32 or 16, the SNR requirement for low BER is increased.

2) PERFORMANCE OF DL DETECTOR TRAINED AT 0 dB

Fig. 16 shows the error performance of the proposed DL-based signal detector for a training SNR of 0 dB. We note that the performance of the proposed DL-based detector with a training SNR of 0 dB is more improved than that with a training SNR of 10 dB. Fig. 16 shows that for a 64-element RIS, infinitesimally low BER is attainable at around -13 dB. For 32- and 16-element RIS, similar BER is attainable at around -10 dB and -7 dB, respectively.

Thus, the training SNR has an impact on the performance of the proposed DL-based detector, and hence, it should be judiciously selected within the operating SNR range. We do not recommend the deep learning-based detector to be trained at negative SNR. This is because the dominant noise at negative SNR may result in higher noise corruption in the training data, impairing the deep neural network's ability to learn the underlying data patterns and leading to some degradation in performance.

3) PERFORMANCE COMPARISONS

The performance of the DL-based detector trained at the two SNRs can be numerically summarized in Table 4. In Table 4, the BER values are rounded up to four decimal points. As observed, the RIS-aided OTFS can provide improved error performance with a large number of RIS processing elements - however, the training SNR has to be judiciously selected.

Finally, we compare the performance of the proposed deep learning (DL)-based detector for RIS-aided OTFS scheme, with the conventional MMSE detector, as depicted in Fig. 17. The results indicate a substantial improvement in the performance of the RIS-assisted OTFS system when equipped with the proposed DL detector. Thus, Fig. 17 demonstrates the efficacy of the proposed DL-based RIS-aided OTFS detector for high-mobility communications. Additionally, Fig. 17 highlights the superiority of the RIS-aided OTFS over the RIS-aided OFDM systems in terms of performance. The former outperforms the latter, as evidenced by Fig. 17. As usual, the performance with a larger number of RIS processing elements is observed to be better than those with fewer elements.

Deep neural network (DNN) based detectors can provide improved performance because they can learn complex signal patterns and classify signals with high accuracy without explicit feature engineering. DNNs adapt to varying signal conditions and generalize to new scenarios, making them more robust and generalizable than traditional signal detection algorithms. They can be trained on a dataset of labeled signals, allowing them to learn the patterns of the signal as well as of the noise for a wide range of signal variations and noise levels. In a nutshell, a DNN-based detector is a promising approach for the signal detection of the RIS-aided OTFS system - it possesses the inherent capability of automatically extracting meaningful features from input signals and it can adaptively detect the signal even in rapidly-changing channel conditions.

C. LIMITATIONS OF THE STUDY AND POTENTIAL FUTURE WORKS

The present study shows that the RIS-aided OTFS system and the proposed DL-based detector have the potential for providing improved performance in the context of next-generation

TABLE 4. The summary of the results for the proposed DL-based detector.

K \ SNR (dB)	-24	-21	-18	-15	-12	-9	-6	-3	0
Model Trained at 0 dB									
64	0.1060	0.0376	0.0065	0.0010	0	0	0	0	0
32	0.2803	0.1633	0.0675	0.0134	0.0013	0	0	0	0
16	0.3766	0.3023	0.2029	0.0942	0.0209	0.0008	0	0	0
Model Trained at 10 dB									
64	0.1149	0.0445	0.0129	0.0031	0.0003	0	0	0	0
32	0.2958	0.1938	0.1040	0.0365	0.0093	0.0021	0	0	0
16	0.4063	0.3537	0.2704	0.1694	0.0788	0.0235	0.0047	0	0

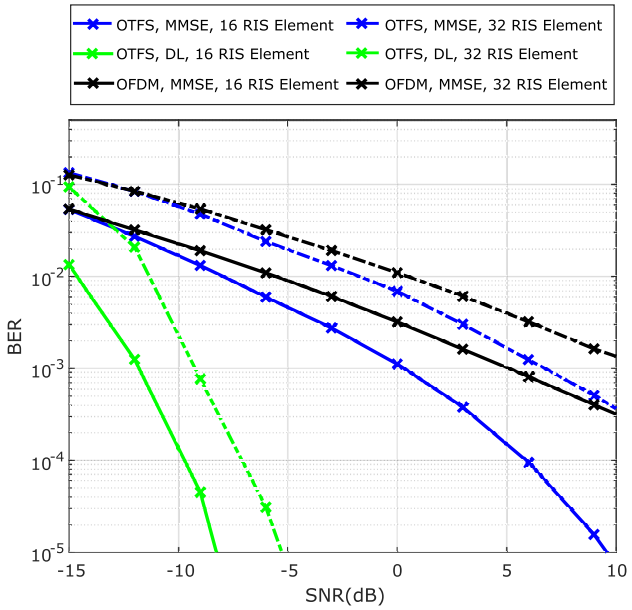

FIGURE 17. Error Performance of the RIS-aided OTFS using the proposed DL-based detector compared with the conventional MMSE detector. The performance is also compared with that of the RIS-aided OFDM scheme.

wireless systems. Nevertheless, the study has got some limitations. As already mentioned, the numerical simulations were conducted using the assumption that the channel state information (CSI) of both the source-to-RIS and the RIS-to-destination links are available at the RIS. Practically, the system will have a pilot overhead to have the instantaneous CSI of both links at the RIS elements. However, since the channel matrices are sparse by nature, the channel estimation might not be too complex [54], [58]. Another limitation of the study is that we employ the RIS-associated reflection-angle control strategy based on the SNR maximization technique presented in [61], [62], and [63]. An improved mechanism for controlling the reflection angles of the RIS elements can be devised for the system [36], [41], [63].

Now, we outline some potential future research ideas related to the present study:

1) RIS-AIDED MIMO-OTFS

The present study deals with single-input single-output (SISO) systems. The RIS-aided MIMO-OTFS designs and the proposed DL-based detector might be useful in the near future. The RIS-aided MIMO-OTFS might have the challenge of fast acquisition of the CSI. The RIS-MIMO-OTFS can also be extended to the RIS-aided massive MIMO-OTFS systems [92], where a three-dimensional DD-domain sparse channel matrix estimation might be feasible.

2) DESIGNING RIS-ASSOCIATED REFLECTION-PHASE CONTROLLERS

The most important task of the RIS is to reflect the signal with an optimized phase shift in order to obtain desirable performance. In addition to the signal processing-based reflection angle controllers [62], [63], some machine learning (ML)-based techniques may also be explored for ensuring an appropriate phase shift toward the desired user. The ML method of controlling the reflection angle of the RIS may also be used for the optimization of resources (power, spectrum, etc.) and for optimized resource allocation among users.

3) RIS-AIDED OTFS FOR JOINT SENSING AND COMMUNICATIONS

One of the key capabilities of next-generation wireless systems will be joint sensing and communications (JSAC), and the waveform design for JSAC is an important research problem. Traditionally, radars use either an un-modulated pulsed signal or a frequency-modulated continuous wave (FMCW) signal for sensing. By contrast, there are different types of modulation for communications. OTFS symbols are mapped to the DD-domain and radar sensing is usually carried out using the Doppler frequency of moving objects, Hence, OTFS-based JSAC has been considered in a few recent works [93], [94]. RIS-aided OTFS can also be a promising candidate for next-generation JSAC. To the best of our knowledge, RIS-aided OTFS for JSAC has not yet been explored.

VI. CONCLUSION

In this paper, we have considered a RIS-aided OTFS scheme for the next-generation high-mobility wireless channels. We have provided a simple matrix multiplication-based input-output relationship for the RIS-aided OTFS. A number of linear and MPA-aided detectors based on the DD-domain channel matrix have been studied, and their performances have been investigated. We have also proposed a DL-based signal detector for the RIS-aided OTFS scheme. A new modality of dataset generation for DL has been conceived. The proposed system exhibits an improved performance using both the conventional and the proposed DL detectors in high-speed doubly selective wireless channels. The proposed DL-based detector can provide infinitesimally low BER at a lower SNR than conventional detectors.

REFERENCES

[1] M. Alsabah, M. A. Naser, B. M. Mahmmod, S. H. Abdulhussain, M. R. Eissa, A. Al-Baidhani, N. K. Noordin, S. M. Sait, K. A. Al-Utaibi, and F. Hashim, "6G wireless communications networks: A comprehensive survey," *IEEE Access*, vol. 9, pp. 148191–148243, 2021.

[2] K. B. Letaief, W. Chen, Y. Shi, J. Zhang, and Y. A. Zhang, "The roadmap to 6G: AI empowered wireless networks," *IEEE Commun. Mag.*, vol. 57, no. 8, pp. 84–90, Aug. 2019.

[3] *Radio Broadcasting Systems: Digital Audio Broadcasting (DAB) to Mobile, Portable and Fixed Receivers*, Standard (ETSI) EN 300 401, ETSI, European Telecommunications Standards Institute, Tech. Rep., May 1997.

[4] *Digital Video Broadcasting: Framing Structure, Channel Coding, and Modulation for Digital Terrestrial Television*, Standard EN 300 744, European Telecommunications Standards Institute, Tech. Rep., Aug. 1997.

[5] *Radio Equipment and Systems, High PErformance Radio Local Area Network (HYPERLAN) Type 1*, Standard (ETSI) ETS 300 652, European Telecommunications Standards Institute, Tech. Rep., Oct. 1996.

[6] T. Y. Al-Naffouri, K. M. Z. Islam, N. Al-Dhahir, and S. Lu, "A model reduction approach for OFDM channel estimation under high mobility conditions," *IEEE Trans. Signal Process.*, vol. 58, no. 4, pp. 2181–2193, Apr. 2010.

[7] L. Hanzo, M. Munster, B. J. Choi, and T. Keller, *OFDM and MC-CDMA for Broadcasting Multi-User Communications, WLANs and Broadcasting*. Hoboken, NJ, USA: Wiley, 2003.

[8] G. L. Stüber, J. R. Barry, S. W. McLaughlin, Y. Li, M. A. Ingram, and T. G. Pratt, "Broadband MIMO-OFDM wireless communications," *Proc. IEEE*, vol. 92, no. 2, pp. 271–294, Feb. 2004.

[9] M. Jiang and L. Hanzo, "Multiuser MIMO-OFDM for next-generation wireless systems," *Proc. IEEE*, vol. 95, no. 7, pp. 1430–1469, Jul. 2007.

[10] B. Farhang-Boroujeny and H. Moradi, "OFDM inspired waveforms for 5G," *IEEE Commun. Surveys Tuts.*, vol. 18, no. 4, pp. 2474–2492, 4th Quart., 2016.

[11] K. T. Truong and R. W. Heath, "Effects of channel aging in massive MIMO systems," *J. Commun. Netw.*, vol. 15, no. 4, pp. 338–351, Aug. 2013.

[12] E. Björnson, J. Hoydis, M. Kountouris, and M. Debbah, "Massive MIMO systems with non-ideal hardware: Energy efficiency, estimation, and capacity limits," *IEEE Trans. Inf. Theory*, vol. 60, no. 11, pp. 7112–7139, Nov. 2014.

[13] A. M. Sayeed and B. Aazhang, "Joint multipath-Doppler diversity in mobile wireless communications," *IEEE Trans. Commun.*, vol. 47, no. 1, pp. 123–132, Jan. 1999.

[14] A. M. Sayeed, A. Sendonaris, and B. Aazhang, "Multiuser detection in fast-fading multipath environments," *IEEE J. Sel. Areas Commun.*, vol. 16, no. 9, pp. 1691–1701, Dec. 1998.

[15] X. Ma and G. B. Giannakis, "Maximum-diversity transmissions over doubly selective wireless channels," *IEEE Trans. Inf. Theory*, vol. 49, no. 7, pp. 1832–1840, Jul. 2003.

[16] X. Ma, G. B. Giannakis, and S. Ohno, "Optimal training for block transmissions over doubly selective wireless fading channels," *IEEE Trans. Signal Process.*, vol. 51, no. 5, pp. 1351–1366, May 2003.

[17] T. Dean, M. Chowdhury, and A. Goldsmith, "A new modulation technique for Doppler compensation in frequency-dispersive channels," in *Proc. IEEE 28th Annu. Int. Symp. Pers., Indoor, Mobile Radio Commun. (PIMRC)*, Oct. 2017, pp. 1–7.

[18] B. Farhang-Boroujeny, "Filter bank spectrum sensing for cognitive radios," *IEEE Trans. Signal Process.*, vol. 56, no. 5, pp. 1801–1811, May 2008.

[19] V. Vakilian, T. Wild, F. Schaich, S. ten Brink, and J.-F. Frigon, "Universal-filtered multi-carrier technique for wireless systems beyond LTE," in *Proc. IEEE Globecom Workshops (GC Wkshps)*, Dec. 2013, pp. 223–228.

[20] G. Fettweis, M. Krondorf, and S. Bittner, "GFDM–Generalized frequency division multiplexing," in *Proc. VTC Spring - IEEE 69th Veh. Technol. Conf.*, Apr. 2009, pp. 1–4.

[21] R. Hadani, S. Rakib, M. Tsatsanis, A. Monk, A. J. Goldsmith, A. F. Molisch, and R. Calderbank, "Orthogonal time frequency space modulation," in *Proc. IEEE Wireless Commun. Netw. Conf. (WCNC)*, Mar. 2017, pp. 1–6, doi: 10.1109/WCNC.2017.7925924.

[22] R. Hadani and A. Monk, "OTFS: A new generation of modulation addressing the challenges of 5G," 2018, *arXiv:1802.02623*.

[23] P. Raviteja, K. T. Phan, Y. Hong, and E. Viterbo, "Interference cancellation and iterative detection for orthogonal time frequency space modulation," *IEEE Trans. Wireless Commun.*, vol. 17, no. 10, pp. 6501–6515, Oct. 2018.

[24] T. Thaj and E. Viterbo, "Low complexity iterative rake decision feedback equalizer for zero-padded OTFS systems," *IEEE Trans. Veh. Technol.*, vol. 69, no. 12, pp. 15606–15622, Dec. 2020.

[25] G. D. Surabhi and A. Chockalingam, "Low-complexity linear equalization for OTFS modulation," *IEEE Commun. Lett.*, vol. 24, no. 2, pp. 330–334, Feb. 2020, doi: 10.1109/LCOMM.2019.2956709.

[26] V. S. Bhat, S. G. Dayanand, and A. Chockalingam, "Performance analysis of OTFS modulation with receive antenna selection," *IEEE Trans. Veh. Technol.*, vol. 70, no. 4, pp. 3382–3395, Apr. 2021, doi: 10.1109/TVT.2021.3063546.

[27] Y. Hong, T. Thaj, and E. Viterbo, *Delay-Doppler Communications: Principles and Applications*. Amsterdam, The Netherlands: Elsevier, 2022.

[28] P. Raviteja, E. Viterbo, and Y. Hong, "OTFS performance on static multipath channels," *IEEE Wireless Commun. Lett.*, vol. 8, no. 3, pp. 745–748, Jun. 2019.

[29] G. D. Surabhi, R. M. Augustine, and A. Chockalingam, "On the diversity of uncoded OTFS modulation in doubly-dispersive channels," *IEEE Trans. Wireless Commun.*, vol. 18, no. 6, pp. 3049–3063, Jun. 2019.

[30] L. Gaudio, G. Colavolpe, and G. Caire, "OTFS vs. OFDM in the presence of sparsity: A fair comparison," *IEEE Trans. Wireless Commun.*, vol. 21, no. 6, pp. 4410–4423, Jun. 2022.

[31] F. Wiffen, L. Sayer, M. Z. Bocus, A. Doufexi, and A. Nix, "Comparison of OTFS and OFDM in ray launched sub-6 GHz and mmWave line-of-sight mobility channels," in *Proc. IEEE 29th Annu. Int. Symp. Pers., Indoor Mobile Radio Commun. (PIMRC)*, Sep. 2018, pp. 73–79.

[32] A. Molisch, *Wireless Communications*. Hoboken, NJ, USA: Wiley, 2005.

[33] M. Patzold, *Mobile Fading Channels*. New York, NY, USA: Wiley, 2003.

[34] E. Basar, "Reconfigurable intelligent surfaces for Doppler effect and multipath fading mitigation," *Frontiers Commun. Netw.*, vol. 2, May 2021, Art. no. 672857.

[35] J. Shaker, M. R. Chaharmir, and J. Ethier, *Reflectarray Antennas: Analysis, Design, Fabrication, and Measurement*. Norwood, MA, USA: Artech House, 2013.

[36] O. Özdogan, E. Björnson, and E. G. Larsson, "Intelligent reflecting surfaces: Physics, propagation, and pathloss modeling," *IEEE Wireless Commun. Lett.*, vol. 9, no. 5, pp. 581–585, May 2020.

[37] N. Yu, "Light propagation with phase discontinuities: Generalized laws of reflection and refraction," *Science*, vol. 334, no. 6054, pp. 333–337, Oct. 2011.

[38] L. Liang, "Anomalous terahertz reflection and scattering by flexible and conformal coding metamaterials," *Adv. Opt. Mater.*, vol. 3, no. 10, pp. 1374–1380, 2015.

[39] Q. Wu and R. Zhang, "Intelligent reflecting surface enhanced wireless network via joint active and passive beamforming," *IEEE Trans. Wireless Commun.*, vol. 18, no. 11, pp. 5394–5409, Nov. 2019.

[40] C. Huang, A. Zappone, G. C. Alexandropoulos, M. Debbah, and C. Yuen, "Reconfigurable intelligent surfaces for energy efficiency in wireless communication," *IEEE Trans. Wireless Commun.*, vol. 18, no. 8, pp. 4157–4170, Aug. 2019.

[41] E. Björnson, Ö. Özdogan, and E. G. Larsson, "Reconfigurable intelligent surfaces: Three myths and two critical questions," *IEEE Commun. Mag.*, vol. 58, no. 12, pp. 90–96, Dec. 2020.

[42] J. Zhang, "Prospective multiple antenna technologies for beyond 5G," *IEEE J. Sel. Areas Commun.*, vol. 38, no. 8, pp. 1637–1660, Aug. 2020.

[43] Q. Wu and R. Zhang, "Towards smart and reconfigurable environment: Intelligent reflecting surface aided wireless network," *IEEE Commun. Mag.*, vol. 58, no. 1, pp. 106–112, Jan. 2020.

[44] E. Bjornson and L. Sanguinetti, "Power scaling laws and near-field behaviors of massive MIMO and intelligent reflecting surfaces," *IEEE Open J. Commun. Soc.*, vol. 1, pp. 1306–1324, 2020.

[45] C. Wang, B. Li, S. Liu, Z. Zhang, and D. Zhao, "1-bit reconfigurable metasurface unit based on resonant coupling," in *Proc. IEEE 5th Int. Conf. Electron. Technol. (ICET)*, May 2022, pp. 79–83.

[46] M. D. Renzo, "Smart radio environments empowered by reconfigurable AI meta-surfaces: An idea whose time has come," *EURASIP J. Wireless Commun. Netw.*, vol. 2019, no. 1, pp. 1–20, Dec. 2019.

[47] Q. Q. Wu and R. Zhang, "Beamforming optimization for wireless network aided by intelligent reflecting surface with discrete phase shifts," *IEEE Trans. Commun.*, vol. 68, no. 3, pp. 1838–1851, May 2020.

[48] O. Ozdogan, E. Bjornson, and E. G. Larsson, "Using intelligent reflecting surfaces for rank improvement in MIMO communications," in *Proc. IEEE Int. Conf. Acoust., Speech Signal Process. (ICASSP)*, May 2020, pp. 9160–9164.

[49] G. Farhadi and N. C. Beaulieu, "On the ergodic capacity of multi-hop wireless relaying systems," *IEEE Trans. Wireless Commun.*, vol. 8, no. 5, pp. 2286–2291, May 2009.

[50] E. Björnson, O. Özdogan, and E. G. Larsson, "Intelligent reflecting surface versus decode-and-forward: How large surfaces are needed to beat relaying?" *IEEE Wireless Commun. Lett.*, vol. 9, no. 2, pp. 244–248, Feb. 2020.

[51] S. Dinh-Van, T. M. Hoang, R. Trestian, and H. X. Nguyen, "Unsupervised deep-learning-based reconfigurable intelligent surface-aided broadcasting communications in industrial IoTs," *IEEE Internet Things J.*, vol. 9, no. 19, pp. 19515–19528, Oct. 2022.

[52] C. Xu, L. Xiang, J. An, C. Dong, S. Sugiura, R. G. Maunder, L.-L. Yang, and L. Hanzo, "OTFS-aided RIS-assisted SAGIN systems outperform their OFDM counterparts in doubly-selective high-Doppler scenarios," *IEEE Internet Things J.*, vol. 10, no. 1, pp. 682–703, Jan. 2023.

[53] V. S. Bhat, G. Harshavardhan, and A. Chockalingam, "Input-output relation and performance of RIS-aided OTFS with fractional delay-Doppler," *IEEE Commun. Lett.*, vol. 27, no. 1, pp. 337–341, Jan. 2023.

[54] A. Naikoti and A. Chockalingam, "Signal detection and channel estimation in OTFS," *ZTE Commun.*, vol. 19, no. 4, pp. 16–33, Dec. 2021.

[55] G. Harshavardhan, V. S. Bhat, and A. Chockalingam, "RIS-aided OTFS modulation in high-Doppler channels," in *Proc. IEEE 33rd Annu. Int. Symp. Pers., Indoor Mobile Radio Commun. (PIMRC)*, Sep. 2022, pp. 409–415.

[56] S. Li, "Hybrid MAP and PIC detection for OTFS modulation," *IEEE Trans. Veh. Technol.*, vol. 70, no. 7, pp. 7193–7198, Jul. 2021.

[57] W. Yuan, Z. Wei, J. Yuan, and D. W. K. Ng, "A simple variational Bayes detector for orthogonal time frequency space (OTFS) modulation," *IEEE Trans. Veh. Technol.*, vol. 69, no. 7, pp. 7976–7980, Apr. 2020.

[58] P. Raviteja, K. T. Phan, and Y. Hong, "Embedded pilot-aided channel estimation for OTFS in delay–Doppler channels," *IEEE Trans. Veh. Tech.*, vol. 68, no. 5, pp. 4906–4917, May 2019.

[59] L. Li, H. Wei, Y. Huang, Y. Yao, W. Ling, G. Chen, P. Li, and Y. Cai, "A simple two-stage equalizer with simplified orthogonal time frequency space modulation over rapidly time-varying channels," 2017, *arXiv:1709.02505*.

[60] P. Raviteja, Y. Hong, E. Viterbo, and E. Biglieri, "Practical pulse-shaping waveforms for reduced-cyclic-prefix OTFS," *IEEE Trans. Veh. Technol.*, vol. 68, no. 1, pp. 957–961, Jan. 2018.

[61] I. Yildirim, E. Basar, and I. F. Akyildiz, "Modeling and analysis of reconfigurable intelligent surfaces for indoor and outdoor applications in future wireless networks," *IEEE Trans. Commun.*, vol. 69, no. 2, pp. 1290–1301, Feb. 2021.

[62] E. Basar, M. Di Renzo, J. De Rosny, M. Debbah, M. Alouini, and R. Zhang, "Wireless communications through reconfigurable intelligent surfaces," *IEEE Access*, vol. 7, pp. 116753–116773, 2019.

[63] E. Björnson, H. Wymeersch, B. Matthiesen, P. Popovski, L. Sanguinetti, and E. de Carvalho, "Reconfigurable intelligent surfaces: A signal processing perspective with wireless applications," *IEEE Signal Process. Mag.*, vol. 39, no. 2, pp. 135–158, Mar. 2022.

[64] A. Naikoti and A. Chockalingam, "Low-complexity delay-Doppler symbol DNN for OTFS signal detection," in *Proc. IEEE 93rd Veh. Technol. Conf. (VTC-Spring)*, Apr. 2021, pp. 1–6.

[65] H. Li, Y. Dong, C. Gong, Z. Zhang, X. Wang, and X. Dai, "Low complexity receiver via expectation propagation for OTFS modulation," *IEEE Commun. Lett.*, vol. 25, no. 10, pp. 3180–3184, Oct. 2021.

[66] H. Zhang and T. Zhang, "A low-complexity message passing detector for OTFS modulation with probability clipping," *IEEE Wireless Commun. Lett.*, vol. 10, no. 6, pp. 1271–1275, Jun. 2021.

[67] P. Raviteja, K. T. Phan, Q. Jin, Y. Hong, and E. Viterbo, "Low-complexity iterative detection for orthogonal time frequency space modulation," in *Proc. IEEE Wireless Commun. Netw. Conf. (WCNC)*, Apr. 2018, pp. 1–6.

[68] Z. Q. Zhang, H. Liu, Q. L. Wang, and P. Fan, "A survey on low complexity detectors for OTFS systems," *ZTE Commun.*, vol. 19, no. 4, pp. 3–15, Dec. 2021.

[69] I. Goodfellow, Y. Bengio, and A. Courville, *Deep Learning*. Cambridge, MA, USA: MIT Press, 2016.

[70] A. Zappone, M. Di Renzo, and M. Debbah, "Wireless networks design in the era of deep learning: Model-based, AI-based, or both?" *IEEE Trans. Commun.*, vol. 67, no. 10, pp. 7331–7376, Oct. 2019.

[71] Y. Qiao, J. Li, B. He, W. Li, and T. Xin, "A novel signal detection scheme based on adaptive ensemble deep learning algorithm in SC-FDE systems," *IEEE Access*, vol. 8, pp. 123514–123523, 2020.

[72] Z. Zhou, L. Liu, J. Xu, and R. Calderbank, "Learning to equalize OTFS," *IEEE Trans. Wireless Commun.*, vol. 21, no. 9, pp. 7723–7736, Sep. 2022.

[73] G. Klambauer, T. Unterthiner, A. Mayr, and S. Hochreiter, "Self-normalizing neural networks," in *Proc. Adv. Neural Inf. Process. Syst.*, vol. 30, 2017, pp. 972–981.

[74] L. Deng and D. Yu, "Deep learning: Methods and applications," *Found. Trends Signal Process.*, vol. 7 nos. 3–4, pp. 197–387, 2013.

[75] A. Rusiecki, "Trimmed categorical cross-entropy for deep learning with label noise," *Electron. Lett.*, vol. 55, no. 6, pp. 319–320, 2019.

[76] Y. LeCun, Y. Bengio, and G. Hinton, "Deep learning," *Nature*, vol. 521, no. 7553, pp. 436–444, Sep. 2015.

[77] A. Géron, *Hands-on Machine Learning With Scikit-Learn, Keras, and TensorFlow*. Sebastopol, CA, USA: O'Reilly Media, 2022.

[78] M. Zinkevich, M. Weimer, L. Li, and A. Smola, "Parallelized stochastic gradient descent," in *Proc. Adv. Neural Inf. Process. Syst.*, vol. 23, 2010, pp. 2595–2603.

[79] A. Kosasih, X. Qu, W. Hardjawana, C. Yue, and B. Vucetic, "Bayesian neural network detector for an orthogonal time frequency space modulation," *IEEE Wireless Commun. Lett.*, vol. 11, no. 12, pp. 2570–2574, Dec. 2022.

[80] T. Wang, C.-K. Wen, H. Wang, F. Gao, T. Jiang, and S. Jin, "Deep learning for wireless physical layer: Opportunities and challenges," *China Commun.*, vol. 14, no. 11, pp. 92–111, Oct. 2017.

[81] T. Erpek, T. J. O'Shea, Y. E. Sagduyu, Y. Shi, and T. C. Clancy, "Deep learning for wireless communications," in *Development and Analysis of Deep Learning Architectures*. Cham, Switzerland: Springer, 2020, pp. 223–266.

[82] X. Yi and C. Zhong, "Deep learning for joint channel estimation and signal detection in OFDM systems," *IEEE Commun. Lett.*, vol. 24, no. 12, pp. 2780–2784, Dec. 2020.

[83] H. Huang, "Deep learning for physical-layer 5G wireless techniques: Opportunities, challenges and solutions," *IEEE Wireless Commun.*, vol. 27, no. 1, pp. 214–222, Feb. 2019.

[84] L. Dai, R. Jiao, F. Adachi, H. V. Poor, and L. Hanzo, "Deep learning for wireless communications: An emerging interdisciplinary paradigm," *IEEE Wireless Commun.*, vol. 27, no. 4, pp. 133–139, Aug. 2020.

[85] C. Luo, J. Ji, Q. Wang, X. Chen, and P. Li, "Channel state information prediction for 5G wireless communications: A deep learning approach," *IEEE Trans. Netw. Sci. Eng.*, vol. 7, no. 1, pp. 227–236, Jan. 2020.

[86] H. Ye, L. Liang, G. Y. Li, and B.-H. F. Juang, "Deep learning-based end-to-end wireless communication systems with conditional GANs as unknown channels," *IEEE Trans. Wireless Commun.*, vol. 19, no. 5, pp. 3133–3143, May 2020.

[87] F. Chollet. (2015). *Keras*. [Online]. Available: https://keras.io

[88] F. Chollet, *Deep Learning With Python*, 2nd ed. Shelter Island, NY, USA: Manning Publications, 2021. [Online]. Available: https://books.google.com.bd/books?id=XHpKEAAAQBAJ

[89] Q. Li, Y. Gong, Y. Liu, and Z. Xu, "Explore the performance of receiver algorithm in OTFS based on DNN," 2022, doi: 10.21203/rs.3.rs-1361868/v1.

[90] X. Ma, Z. Gao, F. Gao, and M. Di Renzo, "Model-driven deep learning based channel estimation and feedback for millimeter-wave massive hybrid MIMO systems," *IEEE J. Sel. Areas Commun.*, vol. 39, no. 8, pp. 2388–2406, Jun. 2021.
[91] P. J. Freire, S. Srivallapanondh, A. Napoli, J. E. Prilepsky, and S. K. Turitsyn, "Computational complexity evaluation of neural network applications in signal processing," 2022, *arXiv:2206.12191*.
[92] M. Li, S. Zhang, P. Fan, and O. A. Dobre, "Multiple access for massive MIMO-OTFS networks over angle-delay-Doppler domain," in *Proc. GLOBECOM IEEE Global Commun. Conf.*, Dec. 2020, pp. 1–6.
[93] L. Gaudio, M. Kobayashi, G. Caire, and G. Colavolpe, "On the effectiveness of OTFS for joint radar parameter estimation and communication," *IEEE Trans. Wireless Commun.*, vol. 19, no. 9, pp. 5951–5965, Sep. 2020.
[94] S. E. Zegrar, S. Rafique, and H. Arslan, "OTFS-FMCW waveform design for low complexity joint sensing and communication," in *Proc. IEEE 33rd Annu. Int. Symp. Pers., Indoor Mobile Radio Commun. (PIMRC)*, Sep. 2022, pp. 988–993.

MAHMUDUL HASAN ABID received the B.Sc. degree in electronics and communication engineering from Khulna University, Bangladesh. He is currently pursuing the M.Sc. degree in electronics and communication engineering with the Engineering Program. He is also with the Electronics and Communication Engineering Discipline, Khulna University. His research interests include wireless communications, machine learning, deep learning, the IoT, and smart grids.

IFFAT ARA TALIN received the B.Sc. degree in electronics and communication engineering from Khulna University, Bangladesh. She is currently pursuing the M.Sc. degree in electronics and communication engineering with the Engineering Program. She is also with the Electronics and Communication Engineering Discipline, Khulna University. Her research interests include next-generation wireless systems, waveform design for future wireless systems, machine learning, deep learning, and smart grids.

MOHAMMAD ISMAT KADIR (Senior Member, IEEE) received the B.Sc. (Eng.) degree in electrical and electronic engineering and the M.Sc. (Eng.) degree in computer engineering from the Bangladesh University of Engineering and Technology, Dhaka, Bangladesh, in 1992 and 1999, respectively, and the Ph.D. degree in electronics and electrical engineering from the University of Southampton, Southampton, U.K., in 2014.

He was a Visiting Fellow with the School of Electronics and Computer Systems (ECS), University of Southampton, from 2016 to 2017. He is currently a Professor with the Electronics and Communication Engineering Discipline, Khulna University, Bangladesh. His research interests include new multi-carrier systems, space-time coding, machine learning for communications, joint sensing, and communications and compressed sensing for wireless communications. He received the Commonwealth Scholarship and the Commonwealth Fellowship from the Commonwealth Scholarship Commission, U.K.